Direct estimates of biomass burning NO_x emissions and lifetimes using daily observations from TROPOMI

Xiaomeng Jin[1], Qindan Zhu[2], Ronald C. Cohen[1,2]

[1]Department of Chemistry, University of California, Berkeley, Berkeley, CA, 94720, United States
[2]Department of Earth and Planetary Science, University of California, Berkeley, Berkeley, CA, 94720, United States

Correspondence to: Xiaomeng Jin (xiaomeng_jin@berkeley.edu) and Ronald C. Cohen (rccohen@berkeley.edu)

Abstract. Biomass burning emits an estimated 25% of global annual nitrogen oxides (NO_x), an important constituent that participates in the oxidative chemistry of the atmosphere. Estimates of NO_x emission factors, representing the amount of NO_x per mass burned, are primarily based on field or laboratory case studies, but the sporadic and transient nature of wildfires makes it challenging to verify whether these case studies represent the behavior of the global fires that occur on earth. Satellite remote sensing provides a unique view of the earth, allowing the study of emissions and downwind evolution of NO_x from a large number of fires. We describe direct estimates of NO_x emissions and lifetimes for fires using an exponentially modified Gaussian analysis of daily TROPOspheric Monitoring Instrument (TROPOMI) retrievals of NO_2 tropospheric columns. We update the *a priori* profile of NO_2 with a fine-resolution (0.25˚) global model simulation from NASA's GEOS Composition Forecasting System (GEOS-CF), which largely enhances NO_2 columns over fire plumes. We derive representative NO_x emission factors for six fuel types globally by linking TROPOMI derived NO_x emissions with observations of fire radiative power from Moderate Resolution Imaging Spectroradiometer (MODIS). Satellite-derived NO_x emission factors are largely consistent with those derived from in-situ measurements. We observe decreasing NO_x lifetime with fire emissions, which we infer is due to the increase in both NO_x abundance and hydroxyl radical production. Our findings suggest promise for applying space-based observations to track the emissions and chemical evolution of reactive nitrogen from wildfires.

1 Introduction

Biomass burning emissions affect global radiative forcing, the hydrological cycle, ecosystem and air quality (e.g., Crutzen and Andreae, 1990; Penner et al., 1992; Johnston et al., 2012; Liu et al., 2014). Biomass burning emits an estimated 25% of global annual nitrogen oxides (NO_x = NO + NO_2), an important constituent that participates in the oxidative chemistry of the atmosphere, leading to the formation of tropospheric ozone (O_3) and secondary aerosols that affect air quality, ecosystem health and climate. Unlike other NO_x sources such as power plants that are persistent and relatively static, the sporadic and transient nature of wildfires makes it challenging to estimate emissions experimentally over wide spatial and temporal scales (Ichoku and Ellison, 2014). Biomass burning emissions inventories used in models are subject to uncertainties in estimates or measurements of the burned area, fuel loadings, combustion efficiency, and also the compound-specific emission factors that

relate the mass of a chemical species emitted to fuel consumption (e.g., Petrenko et al., 2012; Liu et al., 2020; Carter et al., 2020). Current estimates of NO_x emission factors are primarily based on field measurements that sample a few fires over a small region (Yokelson et al., 2007; Alvarado et al., 2010; Lindaas et al., 2021), or laboratory studies that measure fire emissions under controlled conditions (McMeeking et al., 2009; Roberts et al., 2020). These previous studies report large variations of NO_x emission factors, even in a similar ecosystem, which could be due to variation in individual fire conditions, nitrogen content of the fuel burned, or differences in sampling techniques and analysis methods (Andreae, 2019). The NO_x emission factors used in global biomass burning emission inventories also vary (Wiedinmyer et al., 2011; Kaiser et al., 2012; Darmenov and Silva, 2015; van der Werf et al., 2017). These varying perspectives raise the question of how well we understand how to extrapolate the emission factors derived from individual fires to the large number of fires that occur annually on the globe, each with distinct fire conditions, intensity, and fuel type.

Satellite remote sensing provides a unique view of the earth, which offers the opportunity to study a large number of fires globally. Satellite-based products such as fire radiative power (FRP) and burned area have been widely used in the fire detection (Wiedinmyer et al., 2011; van der Werf et al., 2017). The launch of GOME-1 in 1995 set the milestone for monitoring NO_x from space (Richter et al., 2005). The Ozone Monitoring Instrument (OMI) onboard Aura satellite has a finer spatial resolution with 13 ×24 km^2 at nadir, which is widely used to detect NO_x emissions from anthropogenic sources (Beirle et al., 2011; Lu et al., 2015; Duncan et al., 2016; Liu et al., 2016). These studies typically rely on aggregation of multiple observations to reduce the noise of satellite retrievals or improve spatial resolutions via oversampling, tools which cannot be used to study the rapidly varying NO_x from fires. In October 2017, the TROPOspheric Monitoring Instrument (TROPOMI) launched to space (Veefkind et al., 2012). The finer spatial resolution (~7 × 3.5 km^2), and the improved signal-to-noise ratio of TROPOMI compared to OMI offer new opportunities to more reliably interpret observations of individual plumes (Veefkind et al., 2012; Judd et al., 2019; van Geffen et al., 2020).

The accuracy of satellite retrieval of NO_2 columns largely depends on the *a priori* knowledge of NO_2 vertical profile shape needed for calculating air mass factor (e.g., Boersma et al., 2018; Verhoelst et al., 2021). The impacts of the *a priori* profile are especially evident for fire plumes with intense emissions and varying plume dynamics (Bousserez, 2014). Previous studies that use satellite observations to derive NO_x EFs from fires all show lower EFs than *in situ* measurements, which could be due to inaccurate *a priori* profiles (Mebust et al., 2011; Mebust and Cohen, 2014; Schreier et al., 2015). Replacing the *a priori* vertical profile from a fine-resolution regional model can enhance the spatial gradient and correct the low bias of satellite retrieved NO_2 over polluted regions (e.g., Russell et al., 2011; Valin et al., 2011; Goldberg et al., 2017; Ialongo et al., 2020; Judd et al., 2020; Tack et al., 2021). However, conducting fine-resolution simulations for fires distributed globally is currently too computationally expensive for routine analysis. The GEOS Composition Forecasting System (GEOS-CF) produced by NASA Global Modeling and Assimilation Office (GMAO) provides real-time global simulations of atmospheric composition at a fine resolution of 0.25˚ resolution (Keller et al., 2021). The GEOS-CF has provided an opportunity for capturing fine-scale features relevant to biomass burning plumes. Here we apply GEOS-CF simulated NO_2 as the *a priori* profile to re-calculate AMFs for TROPOMI NO_2 columns near fires, and we show updating the *a priori* profile could resolve the underestimate of

satellite-based NO_x emission factors suggested in previous studies (Mebust et al., 2011; Mebust and Cohen, 2014; Schreier et al., 2015).

Satellite instruments observe fire NO_x plumes as a mixture of fresh and aged smoke. NO_x is a short-lived species, and its concentration will decay in the plume due to the formation of nitric acid (HNO_3), peroxyacetyl nitrate (PAN) and organic nitrates ($RONO_2$). The relationship between satellite observed NO_x concentration and emissions depends on the loss rate of NO_x. The chemical processes governing the lifetime of NO_x in the fire plumes are poorly understood (Alvarado et al., 2010). Previous studies assume a constant chemical NO_x lifetime of 2 hours (Mebust et al., 2011; Mebust and Cohen, 2014). Laughner and Cohen (2019) provide space-based evidence of changing NO_x lifetimes over U.S. cities as NO_x emissions decline. As fire intensity varies by several orders of magnitude, assuming constant NO_x lifetime for all fires will likely introduce errors in the derived NO_x emissions (De Foy et al., 2014). The improved spatial resolution of TROPOMI allows direct measurements of the length scale of NO_2 decay. By analyzing the plume evolution downwind, we derive an effective NO_x lifetime. Beirle et al. (2011) first proposed an exponentially modified Gaussian (EMG) approach to directly estimate NO_x emissions and lifetimes from satellite observations, which has been widely used to derive NO_x emissions from anthropogenic sources (Beirle et al., 2011; Lu et al., 2015; Goldberg et al., 2019; Laughner and Cohen, 2019). Our study is the first to apply the EMG approach to simultaneously estimate NO_x emissions and lifetimes from biomass burning plumes. The resulting emission estimates provide a large ensemble with which to evaluate current emission models and also provide detailed constraints on the chemical evolution of NO_x. The resulting lifetimes provide insights into hydroxyl radical abundances in the plume and thus constraints on the lifetime of other chemicals emitted from fires.

2 Datasets

TROPOMI is a nadir-viewing hyperspectral spectrometer launched on October 13, 2017 by the European Space Agency (ESA) for the European Union's Copernicus Sentinel 5 Precursor (S5p) satellite mission. TROPOMI provides afternoon (~ 1:30 PM local time) global observations in the UV−visible−near infrared−shortwave spectra with a fine spatial resolution of 7 × 3.5 km^2 at nadir (increased to 5.5 × 3.5 km^2 since August 2019). We obtain the daily Level-2 TROPOMI retrievals of NO_2 tropospheric column density data from April 2018 to June 2020 from NASA Goddard Earth Sciences (GES) Data and Information Services Center (DISC). The retrieval of the NO_2 tropospheric vertical column includes three steps (van Geffen et al., 2019): (1) retrieval of the total slant column density along the optical path using differential optical absorption spectroscopy (Boersma et al., 2011).; (2) subtraction of the total slant column density from stratospheric NO_2 slant column based on information from a data assimilation system (Boersma et al., 2018); (3) conversion of the tropospheric slant column density to vertical column density using air mass factors (AMFs), which are obtained from radiative transfer calculations that account for the viewing geometry, cloud fraction, surface properties, and the *a priori* vertical profile of NO_2 (Boersma et al., 2018). We include TROPOMI observations with the quality assurance value higher than 0.5, which filter out problematic retrievals but still keep good quality retrievals over cloud (or aerosols). In addition to NO_2, we obtain TROPOMI aerosol layer

height (ALH) or pressure (ALP) data, which provides height information of aerosol layer in the troposphere. Retrieval of ALH or ALP is based on the O_2 absorption band at near-infrared wavelengths between 759 and 770 nm (Graaf et al., 2019). Details of the aerosol layer retrieval algorithms can be found at Graaf et al., (2019) and Nanda et al. (2019).

We use the Moderate Resolution Imaging Spectroradiometer (MODIS) Active Fire products (Collection 6) to provide information on the intensity and location of fires (Giglio et al., 2016), which are available from NASA's Fire Information for Resource Management System (FIRMS). We include daytime MODIS measurements from the Aqua satellite to match with the overpass of TROPOMI. Fire detection from MODIS is performed using a contextual algorithm that measures the infrared radiation from fires (Giglio et al., 2016). Each hotspot is recorded as the center of a ~1 × 1 km^2 pixel that contains one or more fires, and the FRP is estimated via an empirical relationship using the 4μm band brightness temperatures (Kaufman et al., 1998). We group fire pixels whose distances are within 20 km as a single fire event, and the center of the fire is calculated as the mean of fire pixel locations weighted by pixel FRP. To assess the sensitivity to the choice of FRP product, we also process the daytime Suomi NPP Visible Infrared Imaging Radiometer Suite (VIIRS) observations of active fire accessed from NASA's FIRMS. VIIRS fire product uses a similar algorithm as MODIS for fire detection (Schroeder et al., 2014). To assess potential effects of aerosol from plumes on satellite retrieval of NO_2, we acquire the Multi-angle Implementation of Atmospheric Correction (MAIAC) Aerosol Optical Depth (AOD) Level-2 1-km daily gridded product (MCD19A2) from NASA's Earth Observing System Data and Information System (EOSDIS). Details of the retrieval of AOD can be found at Lyapustin et al. (2012, 2018).

The fire episodes are classified based on MODIS detected fire location following the fuel classification in the Global Fire Emission Database (GFED), which is estimated using the MODIS land cover type product and University of Maryland classification scheme (Friedl et al., 2010; van der Werf et al., 2017). We assign the fuel type to grid cells with mixed fuel types based on the dominant fuel type. We follow the definition of GFED, grouping savanna, grassland and shrubland fires as a single herbaceous fuel type. To assess if the NO_x EF varies among these three herbaceous types, we use the 500-m yearly MODIS land cover product (v5) to classify the herbaceous fires based on the dominant land cover type (Friedl et al., 2010).

We use wind fields from the hourly ERA-5 reanalysis data developed by the European Center for Medium-range Weather Forecast (ECMWF), which provides meteorological variables at 0.25˚ × 0.25˚resolution with 37 pressure levels from 1000 hPa to 1 hPa from 1979 to present (Hersbach et al., 2020). We sample ERA-5 wind data closest to the center of each fire episode at the TROPOMI overpass time (~1 PM local time).

3 Methods

3.1 An improved fire *a priori* for TROPOMI NO_2

The *a priori* vertical profiles of NO_2 used in the standard TROPOMI products are obtained from global daily model simulations (TM5) with coarse resolution (1˚) and monthly average biomass burning emissions (Williams et al., 2017). Fires are intrinsically episodic and occur over land areas that are often as small as a few kilometers. Here we re-compute the tropospheric

AMFs using the vertical NO_2 profiles provided by the NASA GEOS-CF simulations with 0.25˚ resolution. GEOS-CF system combines GEOS weather analysis and forecasting system with GEOS-Chem chemistry scheme version 12.0.1 (Bey et al., 2001; Keller et al., 2014, 2021; Long et al., 2015). GEOS-CF includes detailed gas-phase and aerosol chemistry (Knowland et al., 2020; Keller et al., 2021). The near-real-time satellite-based Quick Fire Emission Database (QFED v2.5) is used to provide daily biomass burning emissions (Darmenov and Silva, 2015). In the GEOS-CF system, 65% of biomass burning emissions are distributed within the boundary layer, and the other 35% is distributed evenly between 3.5 and 5.5 km (Fischer et al., 2014). GEOS-CF provides hourly global vertical profiles of NO_2 at 23 pressure levels from 1000 hPa to 10 hPa since 2018.

We sample GEOS-CF products at the time and location of all fire episodes identified. For each episode, we spatially interpolate the GEOS-CF simulated NO_2 profiles to match the resolution of TROPOMI products. The AMF ($AMF_{GC,\ clear}$) for clear sky conditions can be calculated following Eq. (1):

$$AMF_{GC,clear} = \frac{\sum_{surf}^{trop} m_l \times x_{GC,l}}{\sum_{surf}^{trop} x_{GC,l}} \quad (1)$$

where m_l is scattering weight, which is a function of satellite viewing geometry, surface pressure and reflectivity etc.; $x_{GC,l}$ is the GEOS-CF sub-column for layer l. We acquire averaging kernels (AK) from TROPOMI Level-2 products, and we interpolate GEOS-CF vertical profiles to the 34 vertical layers that provide information on AKs. AK is equal to the ratio of the scattering weight to the tropospheric AMFs computed from the *a priori* profile (AMF_a) (Eskes and Boersma, 2003):

$$AK_l = \frac{m_l}{AMF_a} \quad (2)$$

Combining Eq. (1) and Eq. (2) gives Eq. (3):

$$AMF_{GC,clear} = \frac{AMF_a \times \sum_{surf}^{trop} AK_l \times x_{GC,l}}{\sum_{surf}^{trop} x_{GC,l}} \quad (3)$$

Given that AMF_a is the ratio of slant columns to vertical columns, we can relate the vertical columns with GEOS-CF simulated profile ($\Omega_{GC,\ clear}$) to the originally retrieved vertical columns (Ω_a) as Eq. (4):

$$\Omega_{GC,clear} = \Omega_a \times \frac{\sum_{surf}^{trop} x_{GC,l}}{\sum_{surf}^{trop} AK_l \times x_{GC,l}} \quad (4)$$

For partly cloudy scenes, the air mass factor can be written as a linear combination of a clear and cloudy air mass factor (Boersma et al., 2004):

$$AMF_{GC} = f_{cloud} AMF_{GC,cloud} + (1 - f_{cloud}) AMF_{GC,clear} \quad (5)$$

where f_{cloud} is radiance weighed cloud fraction, and $AMF_{GC,\ cloud}$ is essentially the above-cloud component of Eq. (3) (Laughner et al., 2018). Therefore, we revise Eq. (4) for the partly cloudy scene as Eq. (6):

$$\Omega_{GC} = \Omega_a \times \left[(1 - f_{cloud}) \frac{\sum_{surf}^{trop} x_{GC,l}}{\sum_{surf}^{trop} AK_l \times x_{GC,l}} + f_{cloud} \frac{\sum_{cloud}^{trop} x_{GC,l}}{\sum_{cloud}^{trop} AK_l \times x_{GC,l}} \right] \quad (6)$$

3.2 Estimation of emissions and lifetimes of wildfires

We apply an EMG approach to estimate NO_x emissions and lifetime from each fire episode. For each fire episode, we first rotate TROPOMI NO_2 swath data along the wind direction in the range of 200 km around the fire centre, and map the rotated TROPOMI NO_2 column to a regular grid with 0.05˚ resolution by calculating area-weighted average as described in Jin et al. (2020). Next, we integrate the TROPOMI NO_2 columns in the across-wind direction within ±100 km, which gives reduced one-dimensional line densities. The NO_2 line densities (L) are then fitted with an EMG model, which is a convolution of a gaussian shaped emission and an exponential decay function (Beirle et al., 2011; Lu et al., 2015; Laughner and Cohen, 2019) following Eq. (7):

$$L(x|a, x_0, \mu_x, \sigma_x, B) = \frac{a}{x_0} exp\left(\frac{\mu_x}{x_0} + \frac{{\sigma_x}^2}{2{x_0}^2} - \frac{x}{x_0}\right) \phi\left(\frac{x-\mu_x}{\sigma_x} - \frac{\sigma_x}{x_0}\right) + B \quad (7)$$

where x_0 is the e-folding distance that represents the length scale of the NO_2 decay; μ_x is the location of the apparent source relative to the fire centre; σ_x represents the Gaussian smoothing length scale; Φ is a cumulative distribution function; a is a scale factor that represents the observed total number of NO_2 molecules in the fire plumes, and B represents the background NO_2. We use the best guesses for initial values following Laughner and Cohen (2019). The effective NO_2 lifetime ($\boldsymbol{\tau}_{EMG}$) and the estimated NO_x emissions (E_{EMG}) can be calculated from the fitted x_0 and a following Eq. (8) and Eq. (9):

$$\boldsymbol{\tau_{EMG}} = \frac{\boldsymbol{x_0}}{\boldsymbol{w}} \quad (8)$$

$$\boldsymbol{E_{EMG}} = \boldsymbol{\gamma} \times \frac{\boldsymbol{a}}{\boldsymbol{\tau_{EMG}}} \quad (9)$$

where w is the wind speed, and γ is the ratio of NO_x to NO_2. The effective lifetime should represent chemical lifetime of NO_x if the transport speed is uniform, the direction is constant and deposition is negligible (De Foy et al., 2014). Previous studies either use the averaged wind of the first several layers (Beirle et al., 2011; Lu et al., 2015) or choose a constant layer such as 900 hPa (Mebust et al., 2011), but injection height of wildfires varies significantly, especially for large fires which inject emissions into high altitudes (Val Martin et al., 2010). To account for varying injection height, we use TROPOMI ALH as an approximation of the fire injection height instead of assuming a constant layer. We vertically interpolate ERA-5 wind data to the pressure level of aerosol layer. For the fires without valid ALH (~36% of the selected fires), we use 900hPa, as the ALP level for the majority of selected fires is near 900 hPa (see Sect. 4.1). γ is assumed to be 1.32, which is in between measured mean NO_x/NO_2 ratio of 1.50 reported in Akagi et al. (2012) and 1.24 in Juncosa Clahorrano et al. (2021). We assume a constant γ because O_3 and the photolysis rate of NO_2 varies little in the plume, and the time scale for NO and NO_2 to reach steady state is of order 100s (Alvarado and Prinn, 2009). Juncosa Clahorrano et al. (2021) shows the NO_x/NO_2 ranges from 1.15 to 1.50 near the fire centre before 3PM LST, but the median NO_x/NO_2 varies little from centre to plume edge. Mebust et al. (2011) suggest the uncertainty of NO_x/NO_2 is ~20%.

3.3 Idealized plume model

To understand the factors that control the NO_x lifetime, we employ a one-dimensional (1-D) multi-box plume model based on the Python Editable Chemical Atmospheric Numerical Solver (PECANS; Laughner 2019; Laughner and Cohen, 2019). PECANS is a flexible idealized atmospheric chemistry modelling framework that allows for one box to three-dimensional multi-box simulations of atmospheric chemistry with idealized transport. In this study, we set the model to be 1-D with 600 km domain size and 2.5 km resolution, which is analogous to the integrated 1-D NO_2 line density along wind direction. The wind speed is fixed at 5 m/s, and the diffusion coefficients are also fixed at 100 m^2/s following Laughner and Cohen (2019). We assume a simplified set of reactions to represent a chemical condition within the NO_x plume including: (1) the permanent removal of NO_x through the formation of HNO_3 and $RONO_2$; (2) the temporary removal and releases of NO_x by PAN; (3) the instantaneous steady-state relationship between NO and NO_x; and (4) the transport of NO_x along the wind direction. The modelled VOC are lumped into two groups; the first group (hereafter RVOC) do not contribute PAN formation; the second group is modelled as an immediate PAN precursor (hereafter OVOC), specifically acetaldehyde. We include a Gaussian shaped NO_x emission source (expressed in NO) at x=200 km with 6 km in half width. The concentrations for O_3, hydroxyl radical production rate $P(HO_x)$, VOC reactivities, and alkyl nitrate branching ratio are given as model input. The O_3 concentration is fixed at 65 ppbv, which is close to observed mean O_3 concentration near fire plumes (Alvarado and Prinn, 2009; Alvarado et al., 2014). A fixed branching ratio to form $RONO_2$ in RO_2 + NO reaction of 0.05 is used following Laughner and Cohen (2019). We run PECANS repeatedly with varying NO_x emissions, $P(HO_x)$, RVOC, and OVOC. Each model run outputs the concentration of NO_x and its major sinks along the wind direction, which are then used to calculate both EMG fitted and chemical NO_x lifetime.

3.4 Selection of wildfires

Since not all fire plumes are detectable from space, and the EMG approach works best for single sources with clear plume patterns, we apply the following four criteria to select candidate fires from fire plumes identified from MODIS FRP observations (see Fig. S1 for a flowchart of the selection procedure):

First, fires should be large enough so that an apparent enhancement of NO_2 is observed from TROPOMI. Considering the detection limit of TROPOMI NO_2 and the greater uncertainty of MODIS FRP for small fires (Kaufman et al., 1998), fire episodes with MODIS FRP higher than 200 MW are selected. We then select fires where TROPOMI NO_2 tropospheric columns on the fire day are at least one standard deviation higher than the mean TROPOMI NO_2 columns 30 days before and after the fire day (excluding the nearest four days as fires may last for several days, defined as Ω_{NO2_B}). We only include fires in which TROPOMI NO_2 line densities peak near the fire centre, meaning that fires with monotonically increasing or decreasing line densities within the region are excluded.

Second, nearby fire plumes should not contribute to the NO_2 line density of the selected fires. A major challenge of applying the EMG approach is that it only applies to single source, but isolated wildfires are rare in nature. To reduce the influence of

nearby plumes, we develop an algorithm that automatically detects and filters out the surrounding plumes (Fig. S2). We first identify plume-affected grid cells defined as Ω_{NO2} higher than background NO_2 (Ω_{NO2_B}, Fig. S2(b)). Next, pixels are grouped to separate plumes based on their connections with surrounding pixels, assuming that plume pixels belonging to the same fire event should be connected. We then exclude the plumes that do not belong to the centre fire plumes (Fig. S2(c)). The filtered areas are filled with background Ω_{NO2_B} (Fig. S2(d)). The ability of clustering depends on the choice of Ω_{NO2_B}: high Ω_{NO2_B} may truncate plumes as edges are counted as background, while low Ω_{NO2_B} may lead to background being counted as fire plumes, so that nearby plumes are connected with centre plumes. To optimize the performance, we repeat the clustering and filtering steps with different Ω_{NO2_B}, and select the Ω_{NO2_B} that maximizes the filtered size of nearby plumes while retains the centre plume. This filtering algorithm, however, does not apply to the case where fire plumes are overlapped. Therefore, we further exclude the fire plumes where comparable or larger fires are detected (i.e., total FRP of the nearby plumes is greater than one-third of the selected fire) over the region after applying the filtering.

Third, the fire plumes should align with the wind direction. We define a rotation bias as the angle between the wind direction and the observed apparent plume direction. From previous step, we obtain an approximate region of fire plumes, whose coordinates in x and y directions can be fitted with a line using linear regression, where the slope of the line can be converted to degrees (Fig. S3). We only select fire episodes with rotation biases between -30˚ and 30˚.

Fourth, the fire plumes should give good fitting statistics that satisfy the following criteria: 1) $R^2 > 0.5$; 2) $\sigma_x < x_0$, meaning that emission width is smaller than the e-folding distance, which could prevent the case in which emission shape confounds with lifetime; 3) $|\mu_x| < 50$ km, meaning that the apparent source centre is not too far from the fire centre. Fires with more than 50% missing TROPOMI NO_2 values are excluded. The outcome of EMG function is sensitive to the initial condition of each fitting parameter. To test the sensitivity of the fitting results to initial conditions, we repeat the fitting with varying initial values for each parameter 50 times, and we exclude fires where the standard deviation of resulting emissions is more than 50% of the emissions. After excluding the fires sensitive to initial conditions, the uncertainty of the emission due to initial conditions is ~5%.

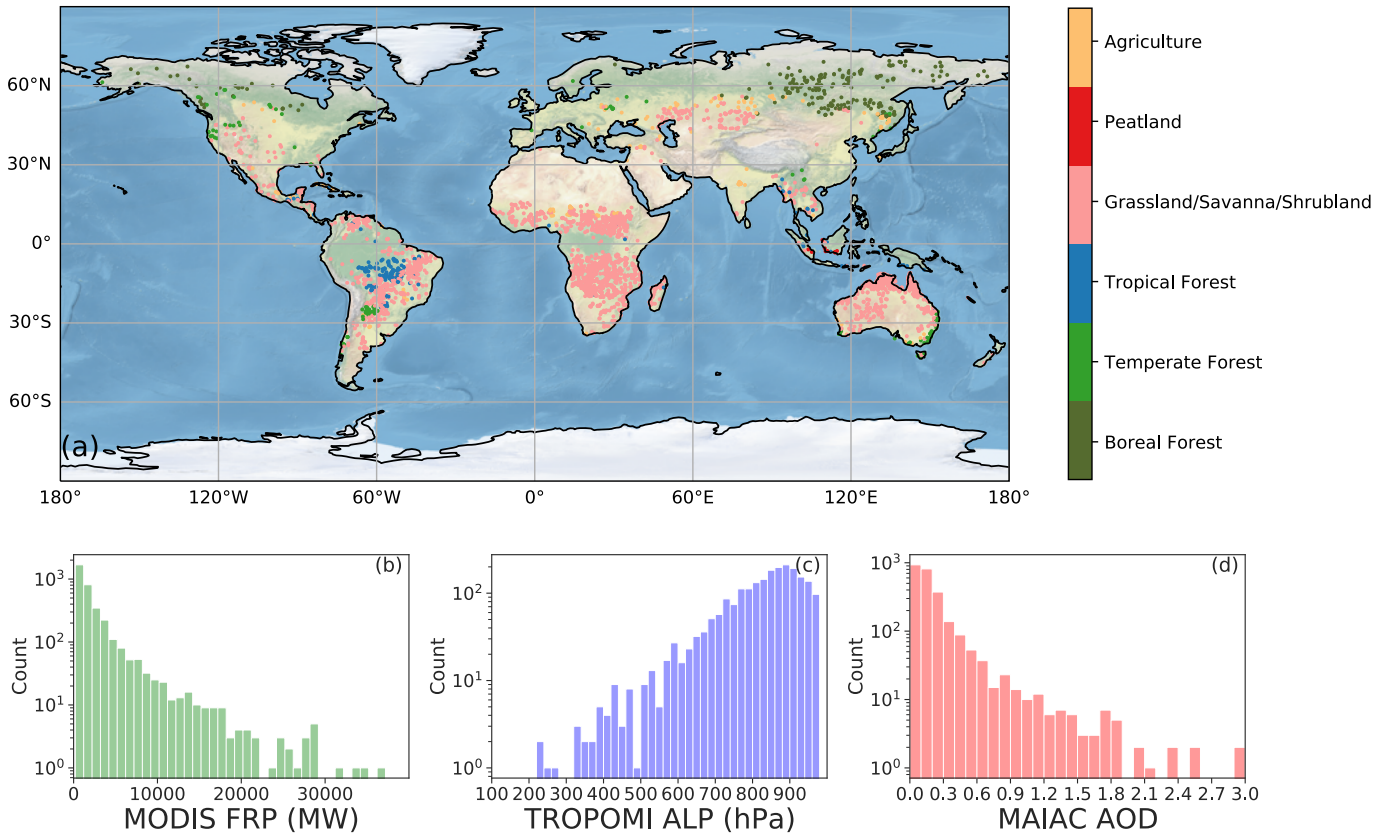

Figure 1 (a) Map of the distribution of selected fire events and corresponding fuel type. Histograms of the distribution of (b) MODIS FRP, (c) TROPOMI ALP, (d) MAIAC AOD for the selected fire events. The number of fire events (y-axis) is on a log scale.

4 Results

4.1 Characteristics of selected fires

Applying above selection criteria, we identified 3248 fire episodes globally between April 2018 and June 2020 suitable for the EMG approach (Fig. 1a). The majority of the fires (77%) occur in the savanna, grassland and shrubland ecosystems. We identified 573 (18%) forest fires, including 227 over the boreal forest, 153 over temperate forest and 193 over the tropical forest fires. Twenty fire episodes are classified as peatland, which occurred in equatorial Asia. We also identified 158 fires (5%) due to agriculture waste burning distributed across different regions. Figures 1b to 1d show the distributions of MODIS FRP, TROPOMI ALP and MAIAC AOD of the selected fire episodes. The MODIS FRP is below 10,000 MW for 95% of the selected fires, and 34 fires have FRP larger than 20,000 MW. The mean TROPOMI ALP is 828 hPa (or 1836 m for ALH), with 1σ standard deviation being 118 hPa (or 1751 m). Assuming TROPOMI ALH is indicative of fire injection height, more than 80% of selected fires inject fire emissions to a pressure level between 700 and 950 hPa. About 83% of the fire episodes

show MAIAC AOD less than 0.3 near the fire centre, and only 64 (3%) fire episodes have AOD higher than 1.0. In summary, most of our selected fires can be characterized as median to large fires with relatively low injection height and small AOD.

4.2 Emission and lifetime estimates with an example fire

We estimate emissions and lifetime for each selected fire episode. As an example, Figure 2 illustrates four major steps to estimate NO_x emissions with a fire event occurred in western Australia (27.98 ˚S, 125.90 ˚E) on October 21, 2018. Several NO_2 plumes are detected by TROPOMI on this day, which outperforms OMI observation on the same day which detects less smaller fires, shows less spatial gradients and larger data gap (Fig. S4). For the fire event selected, we first rotate TROPOMI observations along wind direction (Fig. 2a). Second, we update the *a priori* profile of NO_2 to improve the estimate of NO_2 column (Sect. 3.1), which leads to an enhancement of NO_2 gradient near the fire centre (Fig. 2b). Third, we filter two nearby fire plumes, and the nearby plumes are filled with background NO_2 (Fig. 2c). Fourth, we integrate across the wind direction to obtain a 1-D line density and fit with the EMG function (Fig. 2d and Eqs. (7) to (9)). The EMG model captures the variation of the line density ($R^2 = 0.98$). The lifetime is estimated to be 1.6 hours, and the total NO_x emissions are estimated as 7870 g/s.

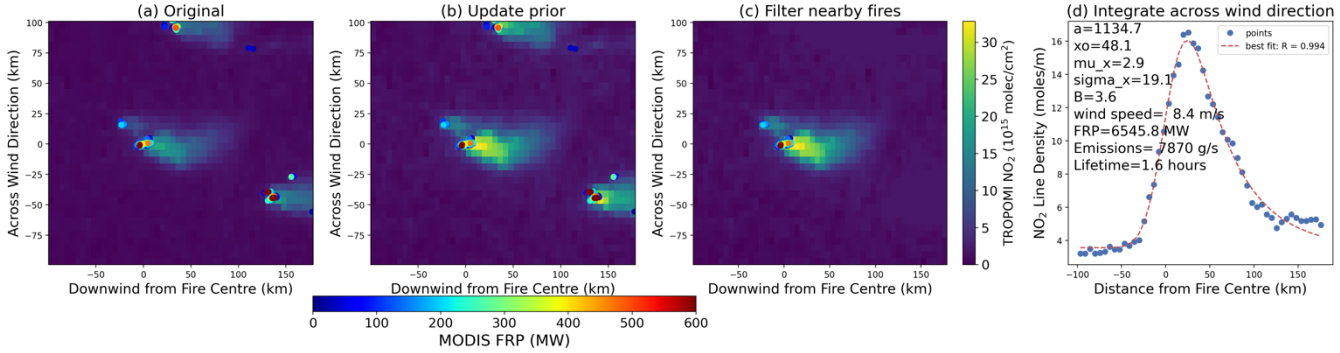

Figure 2 An example fire event illustrating four steps to estimate NO_x emissions and lifetime using the EMG approach: (a) original TROPOMI retrieved NO_2 tropospheric vertical column density rotated to align with the wind direction; (b) retrieved NO_2 column density after replacing the *a priori* vertical profile of NO_2 from NASA GEOS-CF simulation; (c) central fire plume after filtering the nearby fire plumes; (d) NO_2 line density calculated by integrating NO_2 column density across the wind direction. The red line in (d) shows the fitted line density using the EMG function (Eq. (7)). The lifetime is estimated from Eq. (8), and the total NO_x emissions are estimated using Eq. (9). FRP is calculated as the sum of the FPR of all fire pixels detected by MODIS shown on (c).

4.3 Satellite-derived fire NO_x emissions

Deriving NO_x emissions for the large ensemble of fires, we investigate what drives the variation of NO_x emissions and lifetimes among these fires. MODIS FRP, which represents the radiant energy released by fires, has been used to approximate the biomass burned consumption in top-down emission inventories such as Global Fire Assimilation System (GFAS; Kaiser et al., 2012). We define the emission coefficient (EC) as the mass of pollutant emitted per unit of radiative energy (i.e., Emissions/FRP), which has been used to derive the emissions of chemical species from fires (Ichoku and Kaufman, 2005; Mebust et al., 2011; Mebust and Cohen, 2014). Figure 3 shows the relationship between TROPOMI derived NO_x emissions with MODIS FRP for six different fuel types. Overall, we find TROPOMI derived fire NO_x emissions are positively correlated

with MODIS FRP. We assess an overall EC by fitting a line with intercept fixed at zero. FRP explains 39% to 78% variance in emissions with the highest R^2 for tropical forest fires and lowest for agricultural fires. The variability not accounted for may be related to the uncertainty of satellite retrieval of NO_2, errors with the EMG approach, uncertainties with FRP (see Sect. 5), and/or true differences in NO_x ECs for different fires in similar ecosystems. We compute the uncertainty of EC as 95% confidence interval (CI) of the fitted EC based on the Student's *t*-distribution test. Comparing different forest types, EC is largest for tropical forests (1.30 [1.20, 1.40] g/MJ), followed by boreal forests (0.70 [0.60, 0.80] g/MJ) and temperate forests (0.56 [0.47, 0.65] g/MJ). Aggregating all grassland, savanna, and shrubland fires as a single fuel type, we obtain an overall EC of 1.02 [0.98, 1.06] g/MJ. Separating the fires to individual fuel types based on MODIS land cover classification lead to slightly improved R^2 for savanna and grassland, but the derived EC is similar: 1.00 [0.93, 1.07] g/MJ for grassland, 1.13[1.06, 1.19] g/MJ for savanna and 0.89 [0.78, 1.01] g/MJ for shrubland (Fig. S5). Only 20 fires are classified as peatland fires, and we find a relatively good correlation between NO_x emissions and FRP with R^2=0.62 and EC = 0.75 [0.47, 1.03] g/MJ. For agricultural fires, there is a large scatter between NO_x emissions and FRP with R^2 = 0.39, and the estimated EC is 1.10 [0.88, 1.31] g/MJ. Updating the *a priori* profile of NO_2 enhances the spatial gradient of NO_2 (Fig. 2b), allowing for better estimates of fire NO_x emissions. Indeed, we find that using TROPOMI standard products gives a weaker correlation between FRP and NO_x emissions, and the ECs decrease by 46% on average (Fig. S6).

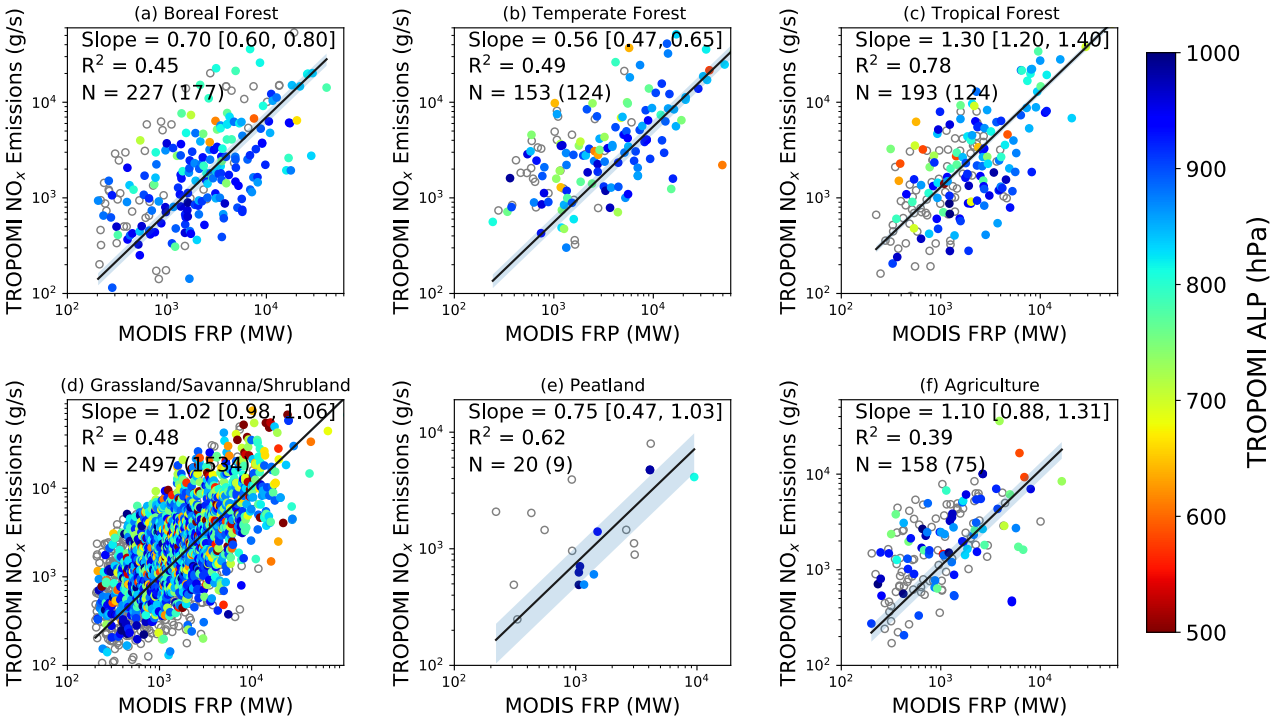

Figure 3 Scatter plots between TROPOMI derived NO_x emissions (g/s) and MODIS FRP (MW) for six fuel types: (a) boreal forest, (b) temperate forest, (c) tropical forest, (d) herbaceous fuel type that combines grassland, savanna and shrubland together, (e) peatland, and (e) agricultural fires. The colours represent the TROPOMI ALP of the corresponding fire events. Fire events without

valid ALP are shown as black circles. The black line indicates the regression line estimated from ordinary least squares with the intercept fixed at zero. The shadow represents the 95% CI of the fitted line, calculated based on the Student's t-distribution test. R^2 is the coefficient of the determination of the linear fit. N is the number of fire events, and the number of fires with valid TROPOMI ALH is in the parenthesis. Emissions and FRP are on log scales.

4.4 Comparison with previous studies

To compare with previous studies, we convert the ECs to emission factors (EFs) assuming a constant ratio of fuel consumption to FRP, $K_r = 0.41$ kg MJ^{-1} (Vermote et al., 2009; Mebust et al., 2011; Mebust and Cohen, 2014). Figure 4 shows the TROPOMI derived NO_x EFs and the associated uncertainties (95% CI) compared to previous studies. We find that satellite-derived NO_x EFs (hereafter EFs_{sat}) are largely consistent with the mean reported in the Andreae (2019, hereafter $EFs_{andreae}$), which represent an up-to-date compilation of field and laboratory measurements over the last two decades. In most fuel types except for temperate forest, EFs_{sat} are largely consistent with $EFs_{andreae}$ to within 30% difference. Our derived NO_x EF_{sat} for tropical forest (3.17 g/kg) is nearly twice as large as that in the boreal forest (1.70 g/kg), consistent with Andreae (2019), which also shows larger NO_x EFs over the tropical forest (2.81 g/kg) than boreal forest (1.18 g/kg). However, for the temperate forest, the derived NO_x EF_{sat} (1.36 g/kg) is less than half of $EF_{andreae}$ (3.02 g/kg). There is a large spread of NO_x EFs for the temperate forests in literature, ranging from 0.49 g/kg (Liu et al., 2017) to 7.44 g/kg (Yokelson et al., 2007). Our derived NO_x EF_{sat}, however, is close to the in-situ estimates of NO_x EFs (1.56 g/kg) from the recent aircraft campaign (i.e., WE-CAN) over the western US during summer 2018 (Lindaas et al., 2021). In non-forest fuel types, we find the smallest NO_x EF_{sat} (1.83 g/kg) over peatland, followed by grassland (2.49 g/kg), and agriculture (2.68 g/kg), which are close to $EF_{andreae}$. Using the standard TROPOMI NO_2 products without updating the *a priori* profile, the derived NO_x EFs are 44 to 66% of EF_{sat}, and 26 to 68% of $EFs_{andreae}$. Assessment of TROPOMI NO_2 with *in situ* measurements also suggest TROPOMI NO_2 is biased low over polluted regions, and replacing the coarse-resolution *a priori* profile with fine-resolution simulations could largely reduce the low biases (Judd et al., 2020; Tack et al., 2021). Our derived NO_x EFs are nearly 3 times larger than a previous study based on OMI observations, which suggest NO_x EFs are lower than 1g/kg in all fuel types (Mebust and Cohen, 2014). Besides the differences in satellite instruments and methods, the discrepancy is partially due to less accurate representation of biomass burning emissions in the *a priori* profile of NO_2 in Mebust and Cohen (2014). Using the standard TROPOMI NO_2 products without updating the *a priori* profile, the derived NO_x EFs are similar to those developed by Mebust and Cohen (2014) for boreal and temperate forest fires, but still higher over other fuel types.

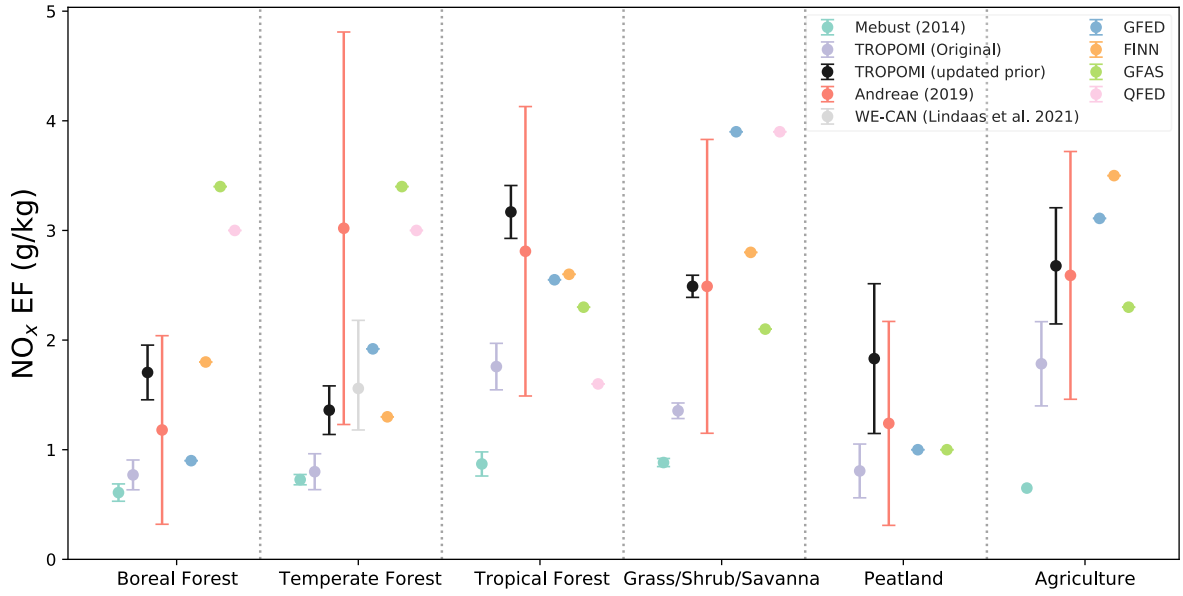

Figure 4 Comparison of the TROPOMI-derived NO_x emission factors with previous studies and those used in global biomass burning emission inventories. We include two estimates of NO_x emission factors: one using the original TROPOMI NO_2 (purple); the other with updated the *a priori* profile for AMF calculation (black). The error bars of TROPOMI NO_x EFs represent 95% CI calculated based on Student's t-distribution test. The red dots show the mean NO_x EFs reported in previous studies compiled by Andreae (2019), and the error bars represent the standard deviation. The error bars of Mebust and Cohen (2014) are calculated using nonparametric bootstrap resampling. The error bars of Lindaas et al. (2021) indicate the overall uncertainty of measurements.

As the development of biomass burning emission inventories is done by separate groups with different approaches, NO_x EFs used in these inventories also differ. We compare our derived NO_x EFs with those used in four commonly used global biomass burning emission inventories (Fig. 4), including: (1) Global Fire Emissions Database (GFED; van der Werf et al., 2017), (2) Fire Inventory from NCAR (FINN; Wiedinmyer et al., 2011), (3) GFAS (Kaiser et al., 2012), and (4) QFED (Darmenov and Silva, 2015). We find that satellite-derived EFs_{sat} best agree with those used in FINN for forest and grassland in terms of absolute magnitude and variations among fuel types. GFED and FINN use smaller EFs over boreal (0.9 g/kg and 1.8 g/kg) and temperate (1.9 g/kg and 1.3 g/kg) forest than tropical forest (2.6 k/kg), which is contrary to GFAS and QFED that use higher NO_x EFs of 3.4 g/kg and 3.0 g/kg for the boreal and temperate forest than that for tropical forest (2.3 and 1.6 g/kg respectively). Our derived NO_x EF_{sat} for tropical forest fires is larger than those used in emission inventories. For grassland, our derived NO_x EF_{sat} of 2.49 g/kg is closest to that used in FINN (2.8 g/kg) and GFAS (2.1 g/kg), and smaller than that used in GFED and QFED (3.9 g/kg). For peatland fires, both GFED and GFAS use EF of 1.0 g/kg, which is smaller than our estimated EF of 1.83 g/kg, but we acknowledge a large uncertainty in our derived EF for peatland given the small number of samples. For agricultural fires, our derived NO_x EF_{sat} (2.68 g/kg) is slightly higher than that used in GFAS (2.3 g/kg), but smaller than that used in GFED (3.11 g/kg) and FINN (3.5 g/kg).

4.5 Satellite-derived NO_x lifetime and its driven factors

We find a large variation of NO_x lifetimes in fire plumes. Figure 5 shows the variation of mean NO_x lifetime as a function of NO_x emissions at different wind speeds. We find an overall negative relationship between NO_x lifetime and emissions: NO_x lifetime decreases from over 5 hours for fires with emissions less than 500 g/s to less than 2 hours for fires higher than 5000 g/s (Fig. 5). We find similar NO_x lifetime using original TROPOMI NO_2 data (Fig. S7), largely because the derived NO_x lifetime is determined by the shape of fire plumes that are not affected by the *a priori*. The varying lifetime with emissions suggests that the assumption of constant lifetime used in previous studies leads to an overestimate in emissions for small fires, while an underestimate of emissions for big fires. At low emission levels (< 2000 g/s), NO_x lifetime tends to decrease with increasing wind speed, which is due to the vertical and horizontal diffusion effects that dilute the concentration of NO_x and thus alters the rate of NO_x removal due to the feedback on OH and the rate of NO_x removal (Valin et al., 2013). However, as NO_x emissions further increase (> 2000 g/s), the chemical removal becomes fast compared to dilution, and NO_x lifetime no longer depends on wind speed (Fig. 5). We note that the EMG derived NO_x emissions depend on both NO_x abundance and lifetime (Eq. (9)), and thus the observed negative emission-lifetime relationship may partially reflect that emissions are estimated from derived NO_x lifetime. However, we find a similar negative relationship between NO_x lifetime and TROPOMI NO_2 column density near the fire centre (Fig. S8), indicating that chemical feedback of NO_x is the primary driver of the derived NO_x lifetime.

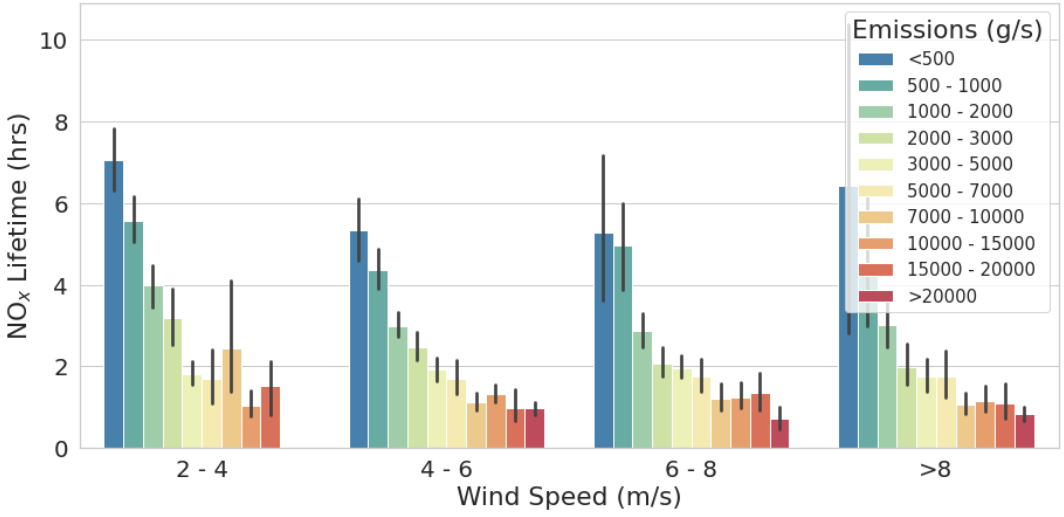

Figure 5 The mean and standard deviation of TROPOMI derived NO_x lifetimes from fires at different emissions (colour) and wind speeds. Fire episodes with less than 2 m/s wind speed are not shown.

The NO_x chemical lifetime, in theory, is determined by its loss to HNO_3 and $RONO_2$. We use the 1-D PECANS model to simulate NO_x evolution downwind fire plumes and calculate a lifetime by fitting model simulated NO_x concentration with the EMG function (Eq. (7)). Figure 6 shows the dependence of the EMG fitted NO_x lifetime on NO_x emissions rate and $P(HO_x)$. At low NO_x emissions, the NO_x lifetime decreases rapidly with increasing NO_x emissions, while almost independent of $P(HO_x)$,

indicating a NO_x-limited regime. At the NO_x-limited regime, increasing NO_x facilitates the conversion from HO_2 to OH, and thus faster loss of NO_x through formation of HNO_3 (e.g., Valin et al., 2014; Romer et al., 2020). The loss of NO_x through formation of $RONO_2$ also increases with NO_x emissions (e.g., Romer et al., 2020). As NO_x emissions further increase, the NO_x lifetime shows a strong dependence on $P(HO_x)$, and the NO_x lifetime increases slightly with NO emissions, indicating a NO_x-saturated regime. In the NO_x-saturated regime, as the loss of NO_x through the formation of HNO_3 consumes both NO_x and OH, increasing NO_x leads to decreasing oxidative capacity and thus a longer NO_x lifetime. If the NO_x lifetime is driven entirely by changes in NO_x concentration, the derived NO_x lifetime should first decrease and then increase with NO_x emissions, which is not found from the observed lifetime-emission relationship. Therefore, we infer that it is likely that $P(HO_x)$ increases with fire intensity in fire plumes, which combined with increasing NO_x abundances, leads to an overall decrease of NO_x lifetime with NO_x emissions. If we assume VOC reactivities and branching ratio α are fixed, we could use TROPOMI retrieved NO_x emissions and lifetimes to infer an approximate level of $P(HO_x)$. Figure 6 labels the satellite retrieved mean NO_x lifetime at a given emission level, and the corresponding $P(HO_x)$. To match the observed negative lifetime-emission relationship, $P(HO_x)$ should also increase by near a factor of 4 from 15×10^6 molec/cm^3 for fires with lifetime longer than 4 hours to 60×10^6 molec/cm^3 for fires with lifetime smaller than 1 hour. The increase in $P(HO_x)$ may be related to increasing emissions of HONO that generate OH. A recent study suggests that previously underestimated HONO emissions from fires are responsible for two-thirds of the HO_x production from fresh fire plumes (Theys et al., 2020). The changes of $P(HO_x)$, however, should be of secondary importance compared to NO_x emissions in driving the observed variations in NO_x lifetime, which can be evidenced from the slower rate of the increase in inferred $P(HO_x)$ and small changes of the NO_x lifetime at high NO_x emissions (Fig. 5).

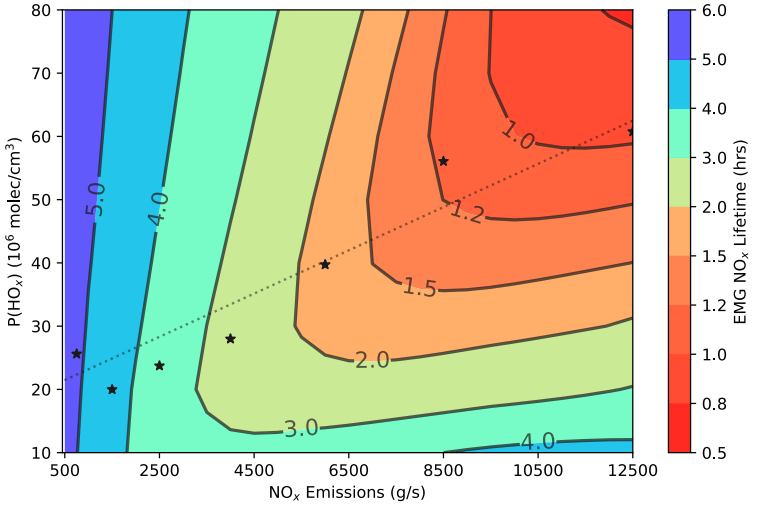

Figure 6 Isopleth showing the NO_x lifetime dependence on NO_x emissions versus $P(HO_x)$. We run the PECANS 1-D model with varying NO_x emissions and $P(HO_x)$. The lifetime is estimated by fitting the modelled NO_x concentration along the wind direction with the EMG function (Eq. (7) and (8)). We run the model at a constant wind speed of 5 m/s, and the VOC reactivity is set constant at 4.8 s^{-1} for both groups (RVOC and OVOC). The black stars show the TROPOMI observed mean NO_x emissions and lifetime at wind speed between 4 to 6 m/s, where the $P(HO_x)$ value is estimated as the level that gives the closest NO_x lifetime as observations at given NO_x emissions. The dashed line represents the fitted regression line.

In addition to NO_x emissions and $P(HO_x)$, VOC reactivity is the third factor that affects the fitted NO_x lifetime. At low NO_x emissions, increasing RVOC reactivity leads to a shorter NO_x lifetime, but its impacts become smaller and reverse with increasing NO_x emissions (Fig. 7a). At low NO_x emissions, increasing RVOC reactivity facilitates the loss of NO_x through the formation of $RONO_2$. At high NO_x emissions, as both RVOC and NO_x consumes OH, increasing VOC leads to a longer NO_x lifetime. The formation of PAN acts as a temporal reservoir of NO_x, which also affects the evolution of NO_x. The formation of PAN depends on the concentration of OVOCs, OH level and temperature. Figure 7b shows the dependence of EMG fitted NO_x lifetime as a function of NO_x emission rate and the reactivity of PAN's immediate precursor (OVOC). We find that increasing PAN formation through increasing OVOC reactivity will lead to an overall increase in EMG fitted NO_x lifetime. The impact of OVOC is especially evident at low levels of NO_x emissions (Fig. 7b). Without PAN formation, the fitted NO_x lifetime will be shorter than that derived from TROPOMI observations, suggesting that PAN formation plays a non-negligible role in determining the evolution of NO_x and also the effective lifetime of NO_x.

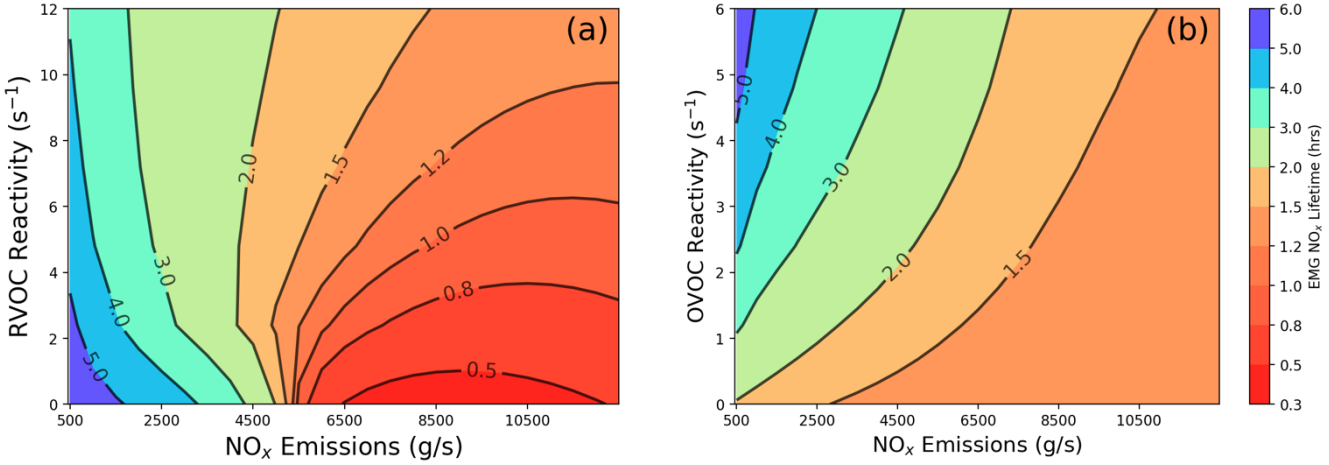

Figure 7 Same as Fig. 6 but showing the NO_x lifetime dependence on NO_x emissions versus the reactivities of (a) RVOC and (b) OVOC. We run the model at a constant wind speed of 5 m/s, and the $P(HO_x)$ is set constant at 50×10^6 molecules/cm^3.

5 Discussions on uncertainties

5.1 Uncertainties of satellite retrieved NO_2 columns

Satellite retrievals of NO_2 columns are subject to uncertainties with spectral fitting, and uncertainties from the *a priori* NO_2 profile shape and scattering weights needed for calculating AMFs and stratospheric NO_2 columns. Boersma et al. (2018) suggest an overall uncertainty of 35% to 45% for single-pixel OMI NO_2 retrieval, which should be smaller for TROPOMI NO_2 given its improved signal-to-noise ratio (van Geffen et al., 2020; Verhoelst et al., 2021). Due to the sporadic nature of fires, there is no validation of TROPOMI NO_2 columns with fire NO_x with ground-based measurements. Validation with ground-based Differential Optical Absorption Spectroscopy (DOAS) and Pandora measurements in urban stations show an overall

good agreement between TROPOMI retrieved and ground-based NO_2 columns, and an overall negative bias is reported, but the biases vary with stations (Lambert et al., 2020; Verhoelst et al., 2021).

Over polluted regions, the uncertainty and bias of single-pixel satellite retrieval of NO_2 columns is dominated by uncertainties of the AMF (Boersma et al., 2018). We replace the *a priori* profile shape of NO_2 using NASA GEOS-CF simulations that include daily biomass burning emissions, which leads to higher NO_x emissions factors that are more consistent with in situ measurements. Bousserez (2014) similarly suggests that using a fire-specific NO_2 profile shape can lead to a near 60% reduction in AMF. In the NASA GEOS-CF, 65% biomass burning emissions are distributed within the boundary layer, which will lead to negative biases in AMF for large fires with plumes that rise well above the boundary layer. In our study, since the ALH is below 2000m for the majority of fires, model uncertainties of the injection height should have small impacts on the retrieval of NO_2 columns. However, we notice that fire events with low ALP (< 700 hPa) tend to show higher NO_x emissions per FRP, and most outliers in Fig. 3 are associated with high aerosol layers. Since satellite instruments are more sensitive to NO_2 at higher altitudes, the inaccurate assumption of NO_2 concentrated within the boundary layer will lead to an underestimate of the AMF and thus an overestimate of the retrieved vertical NO_2 columns if the majority of NO_2 is injected to the free troposphere.

In addition, the large amounts of aerosols emitted from wildfires may also impact the retrieval of NO_2 columns from space. The impacts of aerosols depend on the magnitude, location, and optical properties (absorbing vs. scattering) of aerosols (Bousserez, 2014; Lin et al., 2015). In the TROPOMI NO_2 retrieval algorithm, the effects of aerosols are implicitly accounted for through modifying the cloud properties (Boersma et al., 2011). Bousserez (2014) suggests an explicit correction is needed in the presence of clouds and scattering aerosols, and the effects of aerosol correction can be as large as 100% when cloud fraction is 30% and AOD is higher than 1. In our study, the mean cloud fraction of the selected fire plumes is 9%, and the mean AOD is 0.22, corresponding to a small uncertainty of less than 20% based on Bousserez (2014).

5.2 Uncertainties of MODIS FRP

Since we derive NO_x EFs from the linear regression between TROPOMI NO_x emissions and MODIS FRP, uncertainties in MODIS FRP should also contribute to uncertainties of the satellite derived NO_x EFs. Detection of MODIS FRP may be obscured by cloud, aerosols or canopy cover. The uncertainty of FRP, however, is lower than 5% for fires that aggregate 30 or more active fire pixels together (Freeborn et al., 2014). Our selected fire events are aggregated by 37 active fire pixels on average. To evaluate if our results are robust with the choice of FRP data, we conduct similar analysis with FRP measurements from Suomi NPP VIIRS sensors. In general, MODIS and VIIRS FRP are in good agreement ($R^2 = 0.72$, Fig. S9). VIIRS FRP is lower than MODIS FRP by 5.8% on average. Deriving NO_x emission factors using VIIRS FRP, we find a slight increase of NO_x EFs for forest and agricultural fires, but a decrease for peatland (Fig. S10). For herbaceous fires, where a large number of fires are sampled, the derived NO_x EF remains almost unchanged, suggesting that the difference in MODIS and VIIRS FRP should diminish as we increase the sample size. The overall relationship between NO_x emissions and FRP is similar for both VIIRS and MODIS, though stronger correlation is found for MODIS FRP. Overall, we estimate the difference in NO_x EFs

using MODIS versus VIIRS FRP is ~20%. Here we assume linear relationship between emission rate and FRP. While the validity of the relationship has been verified in laboratory (Wooster et al., 2005; Freeborn et al., 2008), field experiments (Wiggins et al., 2020) and satellite observations (Ichoku and Kaufman, 2005), the choice of the mass-to-energy conversion factor (K_r) slightly differ in Wooster et al. (2005, 0.368 g/MJ) and in Freeborn et al. (2008, 0.453g/MJ), suggesting an uncertainty of order 10% for the value of K_r.

5.3 Uncertainties in the EMG approach

The first step of the EMG approach is to rotate TROPOMI observations along the wind direction. The derived NO_x lifetimes and emissions are therefore subject to uncertainties of the wind direction and speed due to uncertain plume heights that cross wind shear, or the plume thermodynamics that are not captured by ERA5 wind data. In the case the fire plume does not align with wind direction, calculating line density along the wind direction should lead to an underestimate of the *e*-folding distance. In this study, we only select fires with less than 30˚ rotation bias, and the mean rotation bias is 10˚, which corresponds to less than 2% underestimate of the e-folding distance. Uncertainty and variance of the wind speed, however, should lead to errors in the derived NO_x lifetimes. Here we determine the wind speed by interpolating the wind profile to TROPOMI derived aerosol layer. Comparison of TROPOMI ALH with plume height from the Cloud-Aerosol LIdar with Orthogonal Polarization (CALIOP) and the Multi-angle Imaging SpectroRadiometer (MISR) measurements suggest that TROPOMI ALH is overall 500 m lower (Griffin et al., 2020; Nanda et al., 2020). We estimate that an increase of 500 m ALH corresponds to ~22% increase of the wind speed on average, meaning that NO_x lifetime will decrease by ~18%.

Here we use the EMG approach to derive an effective NO_x lifetime of the entire fire plume. Chemical nonlinearities can result in an effective chemical lifetime that is averaged over the plume where at each point in the plume evolution a different chemical lifetime occurs. Besides, the effective lifetime in practice will be confounded by the mixing such as those plume movement in different directions that reduces the line density. To assess if EMG fitted effective NO_x lifetime is indicative of the chemical lifetime, we use the PECANS model to calculate an EMG fitted lifetime and a chemical lifetime of NO_x from two permanent losses of NO_x through the formation of HNO_3 and $RONO_2$ over downwind region (*i.e.*, mean NO_x concentration divided by the mean chemical loss of NO_x). The chemical lifetime of NO_x varies with location (Fig. 8a), which reaches a minimum near the source centre at low NO_x emissions (NO_x-limited regime), but shows maximum at high NO_x emissions (NO_x-saturated regime). The effect of varying lifetime on the emission estimates is not considered with the EMG approach, which instead gives an overall effective NO_x-lifetime of the plume. At low NO_x, the EMG fitted lifetime is higher than the chemical lifetime at the fire centre, but the reverse occurs at high NO_x (Fig. 8a). We notice that the EMG fitted lifetime is overall more consistent with the chemical lifetime around 40 to 50 km downwind from the fire centre, which should vary depending on the model input. Figure 8b compares the EMG fitted lifetime with overall chemical lifetime over downwind regions under different NO_x emissions, $P(HO_x)$ and VOC reactivities. We find a moderate correlation between EMG fitted lifetime and chemical lifetime ($R^2 = 0.37$). If PAN formation is not included, a nearly perfect correlation is found between the EMG fitted and chemical lifetime ($R^2 = 0.93$). In the lower troposphere, PAN is generally considered as a sink of NO_x near the fire, but a source of NO_x

over downwind region, which deepens the gradient of NO_2 near the source but flattens the gradient downwind (Valin et al., 2013). For those large biomass burning events that inject PAN into upper troposphere, PAN acts as a stable reservoir of NO_x, leading to long-range transport of NO_x (Tereszchuk et al., 2013). The EMG approach is unable to capture the effects of PAN formation on the evolution of NO_x as it assumes NO_x decays exponentially. In the presence of PAN formation, we find the EMG approach tends to overestimate NO_x lifetime at low NO_x emission (< 5000 g/s), in which the flattening effect of PAN is more evident, while underestimating NO_x lifetime at high NO_x emissions and low $P(HO_x)$, in which the deepening effect of PAN takes over. Overall, we assess that the overestimate at low NO_x emissions (< 5000 g/s) cause around 33% negative biases to the derived emissions, while 18% positive biases at high NO_x emissions (> 5000 g/s). In-situ measurements show rapid formation of PAN in young smoke within 4 hours of aging, and PAN contributes about 25% of the total reactive nitrogen (Alvarado et al., 2010; Juncosa Calahorrano et al., 2021), suggesting a non-negligible role of PAN as a sink of NO_x near fire source.

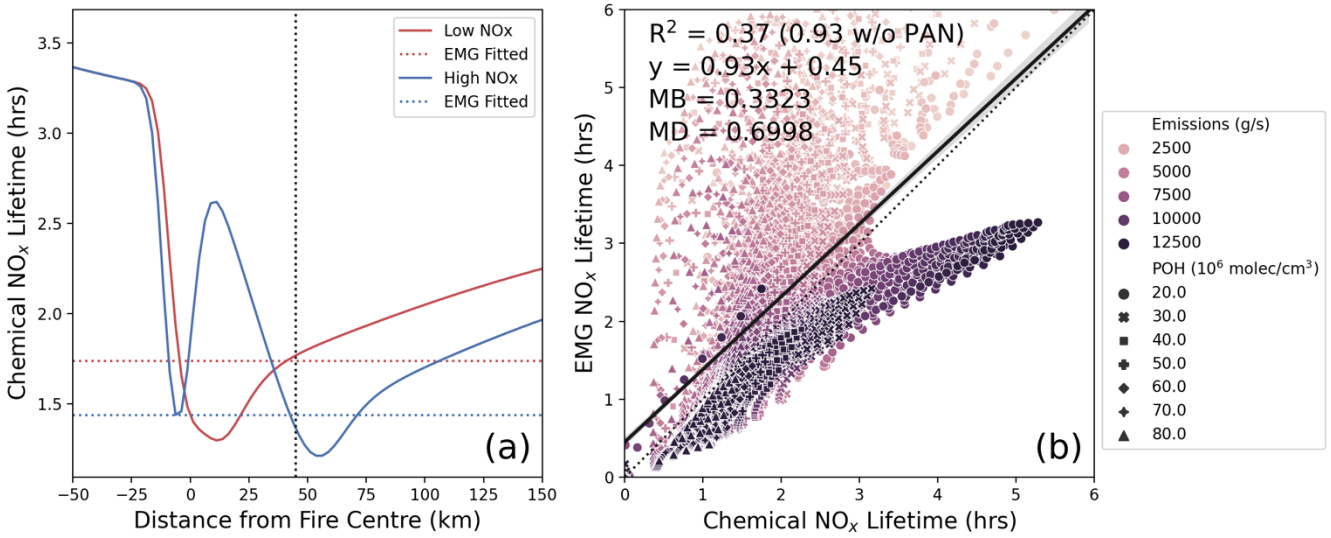

Figure 8 (a) Illustration of the variation of NO_x chemical lifetime with distance from fire centre at both low (red) and high NO_x emissions (blue). The EMG fitted effective lifetime is shown as horizontal dash lines. The vertical line indicates the distance where chemical lifetime and EMG fitted lifetime agree. (b) Scatter plot between EMG fitted versus overall chemical NO_x lifetime downwind calculated using varying NO_x emissions, $P(HO_x)$ and VOC reactivities, where the colours represent different emission levels, and the symbols represent different levels of $P(HO_x)$. The chemical lifetime is calculated as the mean NO_x concentration divided by the mean chemical loss of NO_x through the formation of HNO_3 and $RONO_2$ over downwind region. We define the regional mean as the region between fire centre and the downwind area where NO_x concentration is higher than background, where background value is estimated from the EMG function (B in Eq. (7)).

6 Conclusions

We estimate NO_x emissions and lifetimes from over 3000 fires globally using daily TROPOMI retrievals of NO_2 tropospheric columns, and derive NO_x emission factors by linking TROPOMI derived NO_x emissions with MODIS FRP. The overall derived NO_x emissions factors are 1.70 g/kg, 1.36 g/kg and 3.17 g/kg for the boreal, temperate and tropical forest, 2.49 g/kg

for herbaceous (grassland, savannas and shrubland combined) fires, 1.83 g/kg for peatland, and 2.67 g/kg for agricultural burning. Satellite-derived NO_x emission factors are largely consistent with the mean NO_x emission factors reported by previous field studies (Andreae, 2019). By studying a large number of fires globally, we provide more representative NO_x emission factors. These top-down emission estimates of NO_x could be used to assess biomass burning emission inventories in terms of both emission factors and fuel consumption, which could help diagnose the causes of discrepancies among different emission inventories.

Our study features three improvements over previous studies that use satellite measurements to derive NO_x emissions (Mebust et al., 2011; Mebust and Cohen, 2014; Schreier et al., 2015). First, we use observations from TROPOMI with finer spatial resolution and improved signal-to-noise ratio. Second, we relax the assumptions of constant NO_x lifetime by directly estimating lifetime through fitting the evolution of NO_x downwind with the EMG approach. Third, we replace the *a priori* profile of TROPOMI NO_2 retrieval with a high-resolution global model simulation from NASA GEOS-CF simulations to calculate AMF. This update result in steeper gradients between the plumes and the background, and more accurate description of NO_2 vertical shape, reducing the discrepancy between satellite and in-situ derived estimates of NO_x emission factors. The resolution of current global model simulation, however, is not sufficient to resolve the fine-scale chemical evolution of fire plumes, and better treatment of the fire injection is needed (Paugam et al., 2016). Assessment of the satellite retrieval uncertainty will benefit from high-resolution regional simulations combined with *in situ* measurements that sample individual fire smokes from the point of emission to downwind regions (Juncosa Clahorrano et al., 2021; Lindaas et al., 2020).

We observe decreasing NO_x lifetime with increasing fire NO_x emissions, which is indicative of NO_x-limited chemistry, where increasing NO_x emissions makes the chemical loss of NO_x more efficient. However, for the largest fires with high NO_x, a regime transition from a NO_x-limited to NO_x-saturated regime is expected, where increasing NO_x emissions leads to a longer NO_x lifetime. Using a 1-D idealized plume model to interpret the factors affecting the NO_x lifetime, we infer that $P(HO_x)$ must also increase with fire intensity, consistent with observations that indicate a large source of HONO in fires (Theys et al., 2020; Peng et al., 2020). The formation of PAN also impacts the NO_x lifetime, but the evolution of NO_x due to the formation of PAN and its thermal decomposition over downwind areas is not well captured by the EMG approach that assumes exponential decay with NO_x downwind. Future studies will benefit from the integrative analysis of satellite retrievals of NO_2, HONO and PAN to more completely describe the chemical evolution of reactive nitrogen from wildfires, thus allowing for better prediction of the air quality impacts of fires. TROPOMI is limited to single overpass per day, which cannot resolve the short-term evolution of fire plumes observed by *in situ* measurements (e.g., Juncosa Calahorrano et al., 2021). The newly launched or upcoming geostationary satellite instruments such as GEMS and TEMPO will offer an unprecedented opportunity to continuously observe the emissions and chemical evolution of NO_x from fires that will no longer be limited to a single snapshot (Chance et al., 2013; Kim et al., 2019).

Data and code availability:

TROPOMI NO_2 data (doi:10.5270/S5P-s4ljg54) and TROPOMI ALH (doi:10.5270/S5P-j7aj4gr) are available from NASA Goddard Earth Sciences (GES) Data and Information Services Center (DISC, https://disc.gsfc.nasa.gov/datasets/). MODIS and VIIRS FRP data are available from NASA Earth Data Fire Information for Resource Management Systems (https://earthdata.nasa.gov/earth-observation-data/near-real-time/firms). MAIAC AOD data are available from NASA's Land Processes Distributed Active Archive Center (LP DAAC) located at the USGS Earth Resources Observation and Science (EROS) Center (https://e4ftl01.cr.usgs.gov/MOTA/MCD19A2.006/). ERA5 hourly wind data are available from the Copernicus Climate Service (C3S) Climate Data Store (https://cds.climate.copernicus.eu/cdsapp#!/dataset/reanalysis-era5-pressure-levels). GEOS-CF simulations are available from NASA Global Modeling and Assimilation Office (https://gmao.gsfc.nasa.gov/weather_prediction/GEOS-CF/data_access/). PECANS code is available from https://github.com/joshua-laughner/PECANS .

Acknowledgments:

X. Jin is supported by the NOAA Climate and Global Change Postdoctoral Fellowship Program, administered by UCAR's Cooperative Programs for the Advancement of Earth System Science (CPAESS) under award # NA18NWS4620043B. This work is also supported by NASA Grant 80NSSC18K0624.

Author contribution:

XJ and RC conceived the project. QZ provided the PECANS code. XJ carried out the data analysis and prepared the manuscript with contributions from all co-authors.

Competing interests:

The authors declare that they have no conflict of interest.

References

Akagi, S. K., Craven, J. S., Taylor, J. W., McMeeking, G. R., Yokelson, R. J., Burling, I. R., Urbanski, S. P., Wold, C. E., Seinfeld, J. H., Coe, H., Alvarado, M. J., and Weise, D. R.: Evolution of trace gases and particles emitted by a chaparral fire in California, Atmos Chem Phys, 12, 1397–1421, https://doi.org/10.5194/acp-12-1397-2012, 2012.

Alvarado, M.J., Logan, J.A., Mao, J., Apel, E., Riemer, D., Blake, D., Cohen, R.C., Min, K.E., Perring, A.E., Browne, E.C., Wooldridge, P.J., Diskin, G.S., Sachse, G.W., Fuelberg, H., Sessions, W.R., Harrigan, D.L., Huey, G., Liao, J., Case-

Hanks, A., Jimenez, J.L., Cubison, M.J., Vay, S.A., Weinheimer, A.J., Knapp, D.J., Montzka, D.D., Flocke, F.M., Pollack, I.B., Wennberg, P.O., Kurten, A., Crounse, J., Clair, J.M.S., Wisthaler, A., Mikoviny, T., Yantosca, R.M., Carouge, C.C., Sager, P.L.: Nitrogen oxides and PAN in plumes from boreal fires during ARCTAS-B and their impact on ozone: an integrated analysis of aircraft and satellite observations. Atmospheric Chemistry and Physics, 10, 9739–9760. https://doi.org/10.5194/acp-10-9739-2010, 2010.

Alvarado, M.J., Prinn, R.G.: Formation of ozone and growth of aerosols in young smoke plumes from biomass burning: 1. Lagrangian parcel studies. J Geophys Res Atmospheres, 114, D09306-20. https://doi.org/10.1029/2008jd011144, 2009.

Andreae, M.O.: Emission of trace gases and aerosols from biomass burning – an updated assessment. Atmospheric Chemistry and Physics, 19, 8523–8546. https://doi.org/10.5194/acp-19-8523-2019, 2019.

Beirle, S., Boersma, K.F., Platt, U., Lawrence, M.G., Wagner, T.: Megacity Emissions and Lifetimes of Nitrogen Oxides Probed from Space. Science, 333, 1737–1739. https://doi.org/10.1126/science.1207824, 2011.

Bey, I., Jacob, D.J., Yantosca, R.M., Logan, J.A., Field, B.D., Fiore, A.M., Li, Q., Liu, H.Y., Mickley, L.J., Schultz, M.G.: Global modeling of tropospheric chemistry with assimilated meteorology: Model description and evaluation. J Geophys Res Atmospheres, 106, 23073–23095. https://doi.org/10.1029/2001jd000807, 2001.

Boersma, K.F., Eskes, H.J., Brinksma, E.J.: Error analysis for tropospheric NO2 retrieval from space. Journal of Geophysical Research: Atmospheres (1984–2012), 109, D04311. https://doi.org/10.1029/2003jd003962, 2004.

Boersma, K.F., Eskes, H.J., Dirksen, R.J., A, R.J. van der, Veefkind, J.P., Stammes, P., Huijnen, V., Kleipool, Q.L., Sneep, M., Claas, J., Leitão, J., Richter, A., Zhou, Y., Brunner, D.: An improved tropospheric NO_2 column retrieval algorithm for the Ozone Monitoring Instrument. Atmospheric Measurement Techniques, 4, 1905–1928. https://doi.org/10.5194/amt-4-1905-2011, 2011.

Boersma, K.F., Eskes, H.J., Richter, A., Smedt, I.D., Lorente, A., Beirle, S., Geffen, J.H.G.M. van, Zara, M., Peters, E., Roozendael, M.V., Wagner, T., Maasakkers, J.D., A, R.J. van der, Nightingale, J., Rudder, A.D., Irie, H., Pinardi, G., Lambert, J.-C., Compernolle, S.C.: Improving algorithms and uncertainty estimates for satellite NO2 retrievals: results from the quality assurance for the essential climate variables (QA4ECV) project. Atmospheric Measurement Techniques, 11, 6651–6678. https://doi.org/10.5194/amt-11-6651-2018, 2018.

Bousserez, N.: Space-based retrieval of NO_2 over biomass burning regions: quantifying and reducing uncertainties. Atmospheric Measurement Techniques, 7, 3431–3444. https://doi.org/10.5194/amt-7-3431-2014, 2014.

Carter, T. S., Heald, C. L., Jimenez, J. L., Campuzano-Jost, P., Kondo, Y., Moteki, N., Schwarz, J. P., Wiedinmyer, C., Darmenov, A. S., da Silva, A. M., and Kaiser, J. W.: How emissions uncertainty influences the distribution and radiative impacts of smoke from fires in North America, Atmos. Chem. Phys., 20, 2073–2097, https://doi.org/10.5194/acp-20-2073-2020, 2020.

Chance, K., Liu, X., Suleiman, R.M., Flittner, D.E., Al-Saadi, J., Janz, S.J.: Tropospheric emissions: monitoring of pollution (TEMPO). Proc. SPIE 8866, Earth Observing Systems XVIII, 88660D (September 23, 2013). https://doi.org/10.1117/12.2024479, 2013.

Crutzen, P. J. & Andreae, M. O.: Biomass Burning in the Tropics: Impact on Atmospheric Chemistry and Biogeochemical Cycles. Science, 250, 4988, 1669-1678, https://doi.org/10.1126/science.250.4988.1669, 1990.

Darmenov, A.S., Silva, A. da. The Quick Fire Emissions Dataset (QFED): Technical Report Series on Global Modeling and Data Assimilation, Volume 38, Documentation of versions 2.1, 2.2 and 2.4. https://gmao.gsfc.nasa.gov/pubs/docs/Darmenov796.pdf (last access: April 26, 2021), 2015.

De Foy, B. Wilkins, J.L., Lu, Z., Streets, D.G., Duncan, B.N.: Model evaluation of methods for estimating surface emissions and chemical lifetimes from satellite data. Atmos Environ, 98, 66–77. https://doi.org/10.1016/j.atmosenv.2014.08.051, 2014.

Duncan, B.N., Lamsal, L.N., Thompson, A.M., Yoshida, Y., Lu, Z., Streets, D.G., Hurwitz, M.M., Pickering, K.E.: A space-based, high-resolution view of notable changes in urban NOx pollution around the world (2005-2014). Journal of Geophysical Research: Atmospheresm 121, 976–996. https://doi.org/10.1002/2015jd024121, 2016.

Eskes, H.J., Boersma, K.F.: Averaging kernels for DOAS total-column satellite retrievals. Atmospheric Chemistry and Physics, 3, 1285–1291. https://doi.org/10.5194/acp-3-1285-2003, 2003.

Fischer, E.V., Jacob, D.J., Yantosca, R.M., Sulprizio, M.P., Millet, D.B., Mao, J., Paulot, F., Singh, H.B., Roiger, A., Ries, L., Talbot, R.W., Dzepina, K., Deolal, S.P.: Atmospheric peroxyacetyl nitrate (PAN): a global budget and source attribution. Atmospheric Chemistry and Physics, 14, 2679–2698. https://doi.org/10.5194/acp-14-2679-2014, 2014.

Freeborn, P.H., Wooster, M.J., Hao, W.M., Ryan, C.A., Nordgren, B.L., Baker, S.P., Ichoku, C.: Relationships between energy release, fuel mass loss, and trace gas and aerosol emissions during laboratory biomass fires. J Geophys Res Atmospheres (1984-2012), 113. https://doi.org/10.1029/2007jd008679, 2008.

Freeborn, P.H., Wooster, M.J., Roy, D.P., Cochrane, M.A.: Quantification of MODIS fire radiative power (FRP) measurement uncertainty for use in satellite-based active fire characterization and biomass burning estimation. Geophys Res Lett, 41, 1988–1994. https://doi.org/10.1002/2013gl059086, 2014.

Friedl, M.A., Sulla-Menashe, D., Tan, B., Schneider, A., Ramankutty, N., Sibley, A., Huang, X.: MODIS Collection 5 global land cover: Algorithm refinements and characterization of new datasets. Remote Sensing of Environment, 114, 168–182. https://doi.org/10.1016/j.rse.2009.08.016, 2010.

Giglio, L., Schroeder, W., Justice, C.O.: The collection 6 MODIS active fire detection algorithm and fire products. Remote Sens Environ, 178, 31–41. https://doi.org/10.1016/j.rse.2016.02.054, 2016.

Goldberg, D.L., Lamsal, L.N., Loughner, C.P., Swartz, W.H., Lu, Z., Streets, D.G.: A high-resolution and observationally constrained OMI NO_2 satellite retrieval. Atmos Chem Phys, 17, 11403–11421. https://doi.org/10.5194/acp-17-11403-2017, 2017.

Goldberg, D.L., Lu, Z., Streets, D.G., Foy, B. de, Griffin, D., McLinden, C.A., Lamsal, L.N., Krotkov, N.A., Eskes, H.: Enhanced Capabilities of TROPOMI NO2: Estimating NO_X from North American Cities and Power Plants. Environmental Science & Technology, 53, 12594–12601. https://doi.org/10.1021/acs.est.9b04488, 2019.

Graaf, M. de, Haan, J.F. de, Sanders, A.F.J.: TROPOMI ATBD of the Aerosol Layer Height. http://www.tropomi.eu/sites/default/files/files/publicSentinel-5P-TROPOMI-ATBD-Aerosol-Height.pdf (last access: April 26, 2021), 2019.

Griffin, D., Sioris, C., Chen, J., Dickson, N., Kovachik, A., Graaf, M. de, Nanda, S., Veefkind, P., Dammers, E., McLinden, C.A., Makar, P., Akingunola, A.: The 2018 fire season in North America as seen by TROPOMI: aerosol layer height intercomparisons and evaluation of model-derived plume heights. Atmos Meas Tech, 13, 1427–1445. https://doi.org/10.5194/amt-13-1427-2020, 2020.

Hersbach, H., Bell, B., Berrisford, P., Hirahara, S., Horányi, A., Muñoz-Sabater, J., Nicolas, J., Peubey, C., Radu, R., Schepers, D., Simmons, A., Soci, C., Abdalla, S., Abellan, X., Balsamo, G., Bechtold, P., Biavati, G., Bidlot, J., Bonavita, M., Chiara, G., Dahlgren, P., Dee, D., Diamantakis, M., Dragani, R., Flemming, J., Forbes, R., Fuentes, M., Geer, A., Haimberger, L., Healy, S., Hogan, R.J., Hólm, E., Janisková, M., Keeley, S., Laloyaux, P., Lopez, P., Lupu, C., Radnoti, G., Rosnay, P., Rozum, I., Vamborg, F., Villaume, S., Thépaut, J.: The ERA5 global reanalysis. Q J Roy Meteor Soc, 146, 1999–2049. https://doi.org/10.1002/qj.3803, 2020.

Ichoku, C., Ellison, L. Global top-down smoke-aerosol emissions estimation using satellite fire radiative power measurements. Atmospheric Chemistry and Physics, 14, 6643–6667. https://doi.org/10.5194/acp-14-6643-2014, 2014.

Ichoku, C., Kaufman, Y.J.: A Method to Derive Smoke Emission Rates From MODIS Fire Radiative Energy Measurements. IEEE T Geosci Remote, 43, 2636–2649. https://doi.org/10.1109/tgrs.2005.857328, 2005.

Ialongo, I., Virta, H., Eskes, H., Hovila, J., and Douros, J.: Comparison of TROPOMI/Sentinel-5 Precursor NO_2 observations with ground-based measurements in Helsinki, Atmos. Meas. Tech., 13, 205–218, https://doi.org/10.5194/amt-13-205-2020, 2020.

Jin, X., Fiore, A., Boersma, K.F., Smedt, I.D., Valin, L. Inferring changes in summertime surface ozone-NO_x-VOC chemistry over U.S. urban areas from two decades of satellite and ground-based observations. Environ Sci Technol, 54 (11), 6518-6529, https://doi.org/10.1021/acs.est.9b07785, 2020.

Johnston, F. H., Henderson, S. B., Chen, Y., Randerson, J. T., Marlier, M., DeFries, R. S., Kinney, P., Bowman, D. M.J. S., and Brauer, M.: Estimated global mortality attributable to smoke from landscape fires, Environ. Health Perspect., 120, 695–701, https://doi.org/10.1289/ehp.1104422, 2012.

Judd, L. M., Al-Saadi, J. A., Janz, S. J., Kowalewski, M. G., Pierce, R. B., Szykman, J. J., Valin, L. C., Swap, R., Cede, A., Mueller, M., Tiefengraber, M., Abuhassan, N., and Williams, D.: Evaluating the impact of spatial resolution on tropospheric NO2 column comparisons within urban areas using high-resolution airborne data, Atmos. Meas. Tech., 12, 6091–6111, https://doi.org/10.5194/amt-12-6091-2019, 2019.

Judd, L. M., Al-Saadi, J. A., Szykman, J. J., Valin, L. C., Janz, S. J., Kowalewski, M. G., Eskes, H. J., Veefkind, J. P., Cede, A., Mueller, M., Gebetsberger, M., Swap, R., Pierce, R. B., Nowlan, C. R., Abad, G. G., Nehrir, A., and Williams, D.: Evaluating Sentinel-5P TROPOMI tropospheric NO2 column densities with airborne and Pandora spectrometers near

New York City and Long Island Sound, Atmos. Meas. Tech., 13, 6113–6140, https://doi.org/10.5194/amt-13-6113-2020, 2020.

Juncosa Clahorrano, J., Lindaas, J., O'Dell, K., Palm, B. B., Peng, Q., Flocke, F., Pollack, I. B., Garofalo, L. A., Farmer, D. K., Pierce, J. R., Collett, J. L., Weinheimer, A., Campos, T., Hornbrook, R. S., Hall, S. R., Ullmann, K., Pothier, M. A., Apel, E. C., Permar, W., Hu, L., Hills, A. J., Montzka, D., Tyndall, G., Thornton, J. A., and Fischer, E. V.: Daytime Oxidized Reactive Nitrogen Partitioning in Western U.S. Wildfire Smoke Plumes, J Geophys Res Atmospheres, 126, https://doi.org/10.1029/2020jd033484, 2021.

Kaiser, J.W., Heil, A., Andreae, M.O., Benedetti, A., Chubarova, N., Jones, L., Morcrette, J.J., Razinger, M., Schultz, M.G., Suttie, M., Werf, G.R. van der. Biomass burning emissions estimated with a global fire assimilation system based on observed fire radiative power. Biogeosciences, 9, 527–554. https://doi.org/10.5194/bg-9-527-2012, 2012.

Kaufman, Y.J., Justice, C.O., Flynn, L.P., Kendall, J.D., Prins, E.M., Giglio, L., Ward, D.E., Menzel, W.P., Setzer, A.W.: Potential global fire monitoring from EOS-MODIS. J Geophys Res Atmospheres, 103, 32215–32238. https://doi.org/10.1029/98jd01644, 1998.

Keller, C.A., Knowland, K.E., Duncan, B.N., Liu, J., Anderson, D.C., Das, S., Lucchesi, R.A., Lundgren, E.W., Nicely, J.M., Nielsen, E., Ott, L.E., Saunders, E., Strode, S.A., Wales, P.A., Jacob, D.J., Pawson, S.: Description of the NASA GEOS Composition Forecast Modeling System GEOS-CF v1.0. Journal of Advances in Modeling Earth Systems, 13, e2020MS002413. https://doi. org/10.1029/2020MS002413, 2021.

Keller, C.A., Long, M.S., Yantosca, R.M., Silva, A.M.D., Pawson, S., Jacob, D.J.: HEMCO v1.0: a versatile, ESMF-compliant component for calculating emissions in atmospheric models. Geosci Model Dev, 7, 1409–1417. https://doi.org/10.5194/gmd-7-1409-2014, 2014.

Kim, J., Jeong, U., Ahn, M.-H., Kim, J.H., Park, R.J., Lee, Hanlim, Song, C.H., Choi, Y.-S., Lee, K.-H., Yoo, J.-M., Jeong, M.-J., Park, S.K., Lee, K.-M., Song, C.-K., Kim, Sang-Woo, Kim, Y., Kim, Si-Wan, Kim, M., Go, S., Liu, X., Chance, K., Miller, C.C., Al-Saadi, J., Veihelmann, B., Bhartia, P.K., Torres, O., Abad, G.G., Haffner, D.P., Ko, D.H., Lee, S.H., Woo, J.-H., Chong, H., Park, S.S., Nicks, D., Choi, W.J., Moon, K.-J., Cho, A., Yoon, J., Kim, S., Hong, H., Lee, K., Lee, Hana, Lee, S., Choi, M., Veefkind, P., Levelt, P., Edwards, D.P., Kang, M., Eo, M., Bak, J., Baek, K., Kwon, H.-A., Yang, J., Park, J., Han, K.M., Kim, B.-R., Shin, H.-W., Choi, H., Lee, E., Chong, J., Cha, Y., Koo, J.-H., Irie, H., Hayashida, S., Kasai, Y., Kanaya, Y., Liu, C., Lin, J., Crawford, J.H., Carmichael, G.R., Newchurch, M.J., Lefer, B.L., Herman, J.R., Swap, R.J., Lau, A.K.H., Kurosu, T.P., Jaross, G., Ahlers, B., Dobber, M., McElroy, C.T., Choi, Y.: New Era of Air Quality Monitoring from Space: Geostationary Environment Monitoring Spectrometer (GEMS) New Era of Air Quality Monitoring from Space: Geostationary Environment Monitoring Spectrometer (GEMS). B Am Meteorol Soc, 101, 00. https://doi.org/10.1175/bams-d-18-0013.1, 2019.

Knowland, Keller, C.A., Lucchesi, R.: File Specification for GEOS-CF Product. GMAO Office Note No. 17 (Version 1.1). https://gmao.gsfc.nasa.gov/pubs/docs/Knowland1204.pdf (last access: April 26, 2021), 2020.

Lambert, J.C., Compernolle, S., Eichmann, K.-U., Graaf, M. de, Hubert, D., Keppens, A., Kleipool, Q., Langerock, B., Sha, M.K., Verhoelst, T., Wagner, T., Ahn, C., Argyrouli, A., Balis, D., Chan, K.L., Smedt, I.D., Eskes, H., Fjæraa, A.M., Garane, K., J.F.Gleason, Goutail, F., Granville, J., Hedelt, P., Heue, K.-P., Jaross, G., Koukouli, ML., Landgraf, J., Lutz, R., Nanda, S., Niemeijer, S., Pazmiño, A., Pinardi, G., Pommereau, J.-P., Richter, A., Rozemeijer, N., Sneep, M., SteinZweers, D., Theys, N., Tilstra, G., Torres, O., Valks, P., Geffen, J. van, Vigouroux, C., Wang, P., Weber, M. Quarterly Validation Report of the Copernicus Sentinel-5 Precursor Operational Data Products #09: April 2018 – November 2020. S5P MPC Routine Operations Consolidated Validation Report series. http://www.tropomi.eu/sites/default/files/files/publicS5P-MPC-IASB-ROCVR-02.0.2-20190411_FINAL.pdf (last access: April 26, 2021), 2020.

Laughner, J.L., PECANS (Python Editable Chemical Atmospheric Numeric Solver) Zenodo. doi:10.5281/zenodo.3386652, 2019.

Laughner, J.L., Cohen, R.C.: Direct observation of changing NOx lifetime in North American cities. Science, 366, 723–727. https://doi.org/10.1126/science.aax6832, 2019.

Laughner, J.L., Zhu, Q., Cohen, R.C.: The Berkeley High Resolution Tropospheric NO2 product. Earth Syst Sci Data, 10, 2069–2095. https://doi.org/10.5194/essd-10-2069-2018, 2018.

Lin, J.-T., Liu, M.-Y., Xin, J.-Y., Boersma, K. F., Spurr, R., Martin, R., and Zhang, Q.: Influence of aerosols and surface reflectance on satellite NO_2 retrieval: seasonal and spatial characteristics and implications for NO_x emission constraints, Atmos. Chem. Phys., 15, 11217–11241, https://doi.org/10.5194/acp-15-11217-2015, 2015.

Lindaas, J., Pollack, I.B., Garofalo, L.A., Pothier, M.A., Farmer, D.K., Kreidenweis, S.M., Campos, T.L., Flocke, F., Weinheimer, A.J., Montzka, D.D., Tyndall, G.S., Palm, B.B., Peng, Q., Thornton, J.A., Permar, W., Wielgasz, C., Hu, L., Ottmar, R.D., Restaino, J.C., Hudak, A.T., Ku, I., Zhou, Y., Sive, B.C., Sullivan, A., Collett, J.L., Fischer, E.V.: Emissions of Reactive Nitrogen From Western U.S. Wildfires During Summer 2018. J Geophys Res Atmospheres, 126. https://doi.org/10.1029/2020jd032657, 2021.

Liu, F., Beirle, S., Zhang, Q., Dörner, S., He, K., Wagner, T.: NOx lifetimes and emissions of cities and power plants in polluted background estimated by satellite observations. Atmos Chem Phys, 16, 5283–5298. https://doi.org/10.5194/acp-16-5283-2016, 2016.

Liu, T., Mickley, L.J., Marlier, M.E., DeFries, R.S., Khan, M.F., Latif, M.T., Karambelas, A.: Diagnosing spatial biases and uncertainties in global fire emissions inventories: Indonesia as regional case study. Remote Sens Environ, 237, 111557. https://doi.org/10.1016/j.rse.2019.111557, 2020.

Liu, X., Huey, L.G., Yokelson, R.J., Selimovic, V., Simpson, I.J., Müller, M., Jimenez, J.L., Campuzano-Jost, P., Beyersdorf, A.J., Blake, D.R., Butterfield, Z., Choi, Y., Crounse, J.D., Day, D.A., Diskin, G.S., Dubey, M.K., Fortner, E., Hanisco, T.F., Hu, W., King, L.E., Kleinman, L., Meinardi, S., Mikoviny, T., Onasch, T.B., Palm, B.B., Peischl, J., Pollack, I.B., Ryerson, T.B., Sachse, G.W., Sedlacek, A.J., Shilling, J.E., Springston, S., Clair, J.M.St., Tanner, D.J., Teng, A.P., Wennberg, P.O., Wisthaler, A., Wolfe, G.M.: Airborne measurements of western U.S. wildfire emissions:

Comparison with prescribed burning and air quality implications. J Geophys Res Atmospheres, 122, 6108–6129. https://doi.org/10.1002/2016jd026315, 2017.

Liu, Y., Goodrick, S., Heilman, W.: Wildland fire emissions, carbon, and climate: Wildfire–climate interactions. Forest Ecol Manag, 317, 80–96. https://doi.org/10.1016/j.foreco.2013.02.020, 2014.

Long, M.S., Yantosca, R., Nielsen, J.E., Keller, C.A., Silva, A. da, Sulprizio, M.P., Pawson, S., Jacob, D.J.: Development of a grid-independent GEOS-Chem chemical transport model (v9-02) as an atmospheric chemistry module for Earth system models. Geosci Model Dev, 8, 595–602. https://doi.org/10.5194/gmd-8-595-2015, 2015.

Lu, Z., Streets, D.G., Foy, B. de, Lamsal, L.N., Duncan, B.N., Xing, J.: Emissions of nitrogen oxides from US urban areas: estimation from Ozone Monitoring Instrument retrievals for 2005–2014. Atmospheric Chemistry and Physics, 15, 10367–10383. https://doi.org/10.5194/acp-15-10367-2015, 2015.

Lyapustin, A., Wang, Y., Korkin, S., Huang, D.: MODIS Collection 6 MAIAC Algorithm. Atmospheric Measurement Techniques, 11, 5741–5765, https://doi.org/10.5194/amt-11-5741-2018, 2018.

Lyapustin, A.I., Wang, Y., Laszlo, I., Hilker, T., Hall, F.G., Sellers, P.J., Tucker, C.J., Korkin, S.V.: Multi-angle implementation of atmospheric correction for MODIS (MAIAC): 3. Atmospheric correction. Remote Sensing of Environment, 127, 385–393, 2012.

McMeeking, G.R., Kreidenweis, S.M., Baker, S., Carrico, C.M., Chow, J.C., Collett, J.L., Hao, W.M., Holden, A.S., Kirchstetter, T.W., Malm, W.C., Moosmüller, H., Sullivan, A.P., Wold, C.E.: Emissions of trace gases and aerosols during the open combustion of biomass in the laboratory. J Geophys Res Atmospheres (1984-2012), 114. https://doi.org/10.1029/2009jd011836, 2009.

Mebust, A.K., Cohen, R.C.: Space-based observations of fire NO_x emission coefficients: a global biome-scale comparison. Atmospheric Chemistry and Physics, 14, 2509–2524. https://doi.org/10.5194/acp-14-2509-2014, 2014.

Mebust, A.K., Russell, A.R., Hudman, R.C., Valin, L.C., Cohen, R.C.: Characterization of wildfire NO_x emissions using MODIS fire radiative power and OMI tropospheric NO_2 columns. Atmospheric Chemistry and Physics, 11, 5839–5851. https://doi.org/10.5194/acp-11-5839-2011, 2011.

Nanda, S., Graaf, M. de, Veefkind, J.P., Linden, M. ter, Sneep, M., Haan, J. de, Levelt, P.F.: A neural network radiative transfer model approach applied to the Tropospheric Monitoring Instrument aerosol height algorithm. Atmos Meas Tech, 12, 6619–6634. https://doi.org/10.5194/amt-12-6619-2019, 2019.

Nanda, S., Graaf, M. de, Veefkind, J.P., Sneep, M., Linden, M. ter, Sun, J., Levelt, P.F.: A first comparison of TROPOMI aerosol layer height (ALH) to CALIOP data. Atmos Meas Tech, 13, 3043–3059. https://doi.org/10.5194/amt-13-3043-2020, 2020.

Paugam, R., Wooster, M., Freitas, S., and Val Martin, M.: A review of approaches to estimate wildfire plume injection height within large-scale atmospheric chemical transport models, Atmos. Chem. Phys., 16, 907–925, https://doi.org/10.5194/acp-16-907-2016, 2016.

Peng, Q., Palm, B.B., Melander, K.E., Lee, B.H., Hall, S.R., Ullmann, K., Campos, T., Weinheimer, A.J., Apel, E.C., Hornbrook, R.S., Hills, A.J., Montzka, D.D., Flocke, F., Hu, L., Permar, W., Wielgasz, C., Lindaas, J., Pollack, I.B., Fischer, E.V., Bertram, T.H., Thornton, J.A.: HONO Emissions from Western U.S. Wildfires Provide Dominant Radical Source in Fresh Wildfire Smoke. Environ Sci Technol, 54, 5954–5963. https://doi.org/10.1021/acs.est.0c00126, 2020.

Penner, J. E., Dickinson, R. E. & O'Neill, C. A.: Effects of Aerosol from Biomass Burning on the Global Radiation Budget. Science 256, 1432–1434. http://doi.org/10.1126/science.256.5062.1432, 1992

Petrenko, M., Kahn, R., Chin, M., Soja, A., Kucsera, T., and Harshvardhan: The use of satellite-measured aerosol optical depth to constrain biomass burning emissions source strength in the global model GOCART, J. Geophys. Res., 117, D18212, https://doi.org/10.1029/2012jd017870, 2012.

Richter, A., Burrows, J.P., Nüß, H., Granier, C., Niemeier, U.: Increase in tropospheric nitrogen dioxide over China observed from space. Nature, 437, 129–132. https://doi.org/10.1038/nature04092, 2005.

Roberts, J.M., Stockwell, C.E., Yokelson, R.J., Gouw, J. de, Liu, Y., Selimovic, V., Koss, A.R., Sekimoto, K., Coggon, M.M., Yuan, B., Zarzana, K.J., Brown, S.S., Santin, C., Doerr, S.H., Warneke, C: The nitrogen budget of laboratory-simulated western US wildfires during the FIREX 2016 Fire Lab study. Atmos Chem Phys, 20, 8807–8826. https://doi.org/10.5194/acp-20-8807-2020, 2020.

Romer, P. S., Zare, A., and Cohen, R. C.: The changing role of organic nitrates in the removal and transport of NOx, Atmos. Chem. Phys., 20, 267–279, https://doi.org/10.5194/acp-20-267-2020, 2020.

Russell, A.R., Perring, A.E., Valin, L.C., 2011. Russell, A.R., Perring, A.E., Valin, L.C. A high spatial resolution retrieval of NO2 column densities from OMI: method and evaluation, Atmos. Chem. Phys., 11, 8543–8554, https://doi.org/10.5194/acp-11-8543-2011, 2011.

Schreier, S.F., Richter, A., Schepaschenko, D., Shvidenko, A., Hilboll, A., Burrows, J.P.: Differences in satellite-derived NOx emission factors between Eurasian and North American boreal forest fires. Atmos Environ, 121, 55–65. https://doi.org/10.1016/j.atmosenv.2014.08.071, 2015.

Schroeder, W., Oliva, P., Giglio, L., Csiszar, I.A.: The New VIIRS 375m active fire detection data product: Algorithm description and initial assessment. Remote Sens Environ, 143, 85–96. https://doi.org/10.1016/j.rse.2013.12.008, 2014.

Tack, F., Merlaud, A., Iordache, M.-D., Pinardi, G., Dimitropoulou, E., Eskes, H., Bomans, B., Veefkind, P., and Van Roozendael, M.: Assessment of the TROPOMI tropospheric NO_2 product based on airborne APEX observations, Atmos. Meas. Tech., 14, 615–646, https://doi.org/10.5194/amt-14-615-2021, 2021

Tereszchuk, K. A., Moore, D. P., Harrison, J. J., Boone, C. D., Park, M., Remedios, J. J., Randel, W. J., and Bernath, P. F.: Observations of peroxyacetyl nitrate (PAN) in the upper troposphere by the Atmospheric Chemistry Experiment-Fourier Transform Spectrometer (ACE-FTS), Atmos. Chem. Phys., 13, 5601–5613, https://doi.org/10.5194/acp-13-5601-2013, 2013.

Theys, N., Volkamer, R., Müller, J.-F., Zarzana, K.J., Kille, N., Clarisse, L., Smedt, I.D., Lerot, C., Finkenzeller, H., Hendrick, F., Koenig, T.K., Lee, C.F., Knote, C., Yu, H., Roozendael, M.V.: Global nitrous acid emissions and levels of regional oxidants enhanced by wildfires. Nat Geosci, 1–6. https://doi.org/10.1038/s41561-020-0637-7, 2020.

Val Martin, M.V., Logan, J.A., Kahn, R.A., Leung, F.-Y., Nelson, D.L., Diner, D.J.: Smoke injection heights from fires in North America: analysis of 5 years of satellite observations. Atmos Chem Phys, 10, 1491–1510. https://doi.org/10.5194/acp-10-1491-2010, 2010.

Valin, L.C., Russell, A.R., Cohen, R.C.: Chemical feedback effects on the spatial patterns of the NO_x weekend effect: a sensitivity analysis. Atmospheric Chemistry and Physics, 14, 1–9. https://doi.org/10.5194/acp-14-1-2014, 2014.

Valin, L.C., Russell, A.R., Cohen, R.C.: Variations of OH radical in an urban plume inferred from NO 2column measurements. Geophysical Research Letters, 40, 1856–1860. https://doi.org/10.1002/grl.50267, 2013.

Valin, L.C., Russell, A.R., Hudman, R.C., Cohen, R.C.: Effects of model resolution on the interpretation of satellite NO_2 observations. Atmospheric Chemistry and Physics, 11, 11647–11655. https://doi.org/10.5194/acp-11-11647-2011, 2011.

van der Werf, Guido R. van der, Randerson, J.T., Giglio, L., Leeuwen, T.T. van, Chen, Y., Rogers, B.M., Mu, M., Marle, M.J.E. van, Morton, D.C., Collatz, G.J., Yokelson, R.J., Kasibhatla, P.S.: Global fire emissions estimates during 1997–2016. Earth Syst Sci Data, 9, 697–720. https://doi.org/10.5194/essd-9-697-2017, 2017.

van Geffen, J., Boersma, K. F., Eskes, H., Sneep, M., ter Linden, M., Zara, M., and Veefkind, J. P.: S5P TROPOMI NO2 slant column retrieval: method, stability, uncertainties and comparisons with OMI, Atmos. Meas. Tech., 13, 1315–1335, https://doi.org/10.5194/amt-13-1315-2020, 2020.

van Geffen, J. H. G. M., Eskes, H. J., Boersma, K. F., Maasakkers, J. D., and Veefkind, J. P.: TROPOMI ATBD of the total and tropospheric NO_2 data products (issue 1.4.0), Royal Netherlands Meteorological Institute (KNMI), De Bilt, the Netherlands, 2019.

Veefkind, J.P., Aben, I., McMullan, K., Förster, H., Vries, J. de, Otter, G., Claas, J., Eskes, H.J., Haan, J.F. de, Kleipool, Q., Weele, M. van, Hasekamp, O., Hoogeveen, R., Landgraf, J., Snel, R., Tol, P., Ingmann, P., Voors, R., Kruizinga, B., Vink, R., Visser, H., Levelt, P.F.: TROPOMI on the ESA Sentinel-5 Precursor: A GMES mission for global observations of the atmospheric composition for climate, air quality and ozone layer applications. Remote Sensing of Environment, 120, 70–83. https://doi.org/10.1016/j.rse.2011.09.027, 2012.

Verhoelst, T., Compernolle, S., Pinardi, G., Lambert, J.-C., Eskes, H. J., Eichmann, K.-U., Fjæraa, A. M., Granville, J., Niemeijer, S., Cede, A., Tiefengraber, M., Hendrick, F., Pazmiño, A., Bais, A., Bazureau, A., Boersma, K. F., Bognar, K., Dehn, A., Donner, S., Elokhov, A., Gebetsberger, M., Goutail, F., Grutter de la Mora, M., Gruzdev, A., Gratsea, M., Hansen, G. H., Irie, H., Jepsen, N., Kanaya, Y., Karagkiozidis, D., Kivi, R., Kreher, K., Levelt, P. F., Liu, C., Müller, M., Navarro Comas, M., Piters, A. J. M., Pommereau, J.-P., Portafaix, T., Prados-Roman, C., Puentedura, O., Querel, R., Remmers, J., Richter, A., Rimmer, J., Rivera Cárdenas, C., Saavedra de Miguel, L., Sinyakov, V. P., Stremme, W., Strong, K., Van Roozendael, M., Veefkind, J. P., Wagner, T., Wittrock, F., Yela González, M., and Zehner, C.: Ground-based validation of the Copernicus Sentinel-5P TROPOMI NO2 measurements with the NDACC ZSL-DOAS, MAX-

DOAS and Pandonia global networks, Atmos. Meas. Tech., 14, 481–510, https://doi.org/10.5194/amt-14-481-2021, 2021.

Vermote, E., Ellicott, E., Dubovik, O., Lapyonok, T., Chin, M., Giglio, L., Roberts, G.J.: An approach to estimate global biomass burning emissions of organic and black carbon from MODIS fire radiative power. J Geophys Res Atmospheres (1984-2012), 114. https://doi.org/10.1029/2008jd011188, 2009.

Wiedinmyer, C., Akagi, S.K., Yokelson, R.J., Emmons, L.K., Al-Saadi, J.A., Orlando, J.J., Soja, A.J.: The Fire INventory from NCAR (FINN): a high resolution global model to estimate the emissions from open burning. Geoscientific Model Development, 4, 625–641. https://doi.org/10.5194/gmd-4-625-2011, 2011.

Wiggins, E. B., Soja, A. J., Gargulinski, E., Halliday, H. S., Pierce, R. B., Schmidt, C. C., Nowak, J. B., DiGangi, J. P., Diskin, G. S., Katich, J. M., Perring, A. E., Schwarz, J. P., Anderson, B. E., Chen, G., Crosbie, E. C., Jordan, C., Robinson, C. E., Sanchez, K. J., Shingler, T. J., Shook, M., Thornhill, K. L., Winstead, E. L., Ziemba, L. D., and Moore, R. H.: High Temporal Resolution Satellite Observations of Fire Radiative Power Reveal Link Between Fire Behavior and Aerosol and Gas Emissions, Geophys Res Lett, 47, https://doi.org/10.1029/2020gl090707, 2020.

Williams, J.E., Boersma, K.F., Sager, P.L., Verstraeten, W.W.: The high-resolution version of TM5-MP for optimized satellite retrievals: description and validation. Geosci Model Dev, 10, 721–750. https://doi.org/10.5194/gmd-10-721-2017, 2017.

Wooster, M.J., Roberts, G., Perry, G.L.W., Kaufman, Y.J.: Retrieval of biomass combustion rates and totals from fire radiative power observations: FRP derivation and calibration relationships between biomass consumption and fire radiative energy release. Journal of Geophysical Research, 110, 349–24. https://doi.org/10.1029/2005jd006318, 2005.

Yokelson, R.J., Urbanski, S.P., Atlas, E.L., Toohey, D.W., Alvarado, E.C., Crounse, J.D., Wennberg, P.O., Fisher, M.E., Wold, C.E., Campos, T.L., Adachi, K., Buseck, P.R., Hao, W.M.: Emissions from forest fires near Mexico City. Atmos Chem Phys, 7, 5569–5584. https://doi.org/10.5194/acp-7-5569-2007, 2007.